AD_____

Award Number: W81XWH-06-1-0482

TITLE: Targeting Therapy Resistant Tumor Vessels

PRINCIPAL INVESTIGATOR: Erkki Ruoslahti

CONTRACTING ORGANIZATION: The Burnham Institute
La Jolla, CA 92037

REPORT DATE: May 2007

TYPE OF REPORT: Annual

PREPARED FOR: U.S. Army Medical Research and Materiel Command
Fort Detrick, Maryland 21702-5012

REPORT DOCUMENTATION PAGE

Form Approved
OMB No. 0704-0188

1. REPORT DATE	2. REPORT TYPE	3. DATES COVERED
01-05-2007	Annual	1 May 2006 – 1 May 2007

4. TITLE AND SUBTITLE

Targeting Therapy Resistant Tumor Vessels

5a. CONTRACT NUMBER

5b. GRANT NUMBER
W81XWH-06-1-0482

5c. PROGRAM ELEMENT NUMBER

6. AUTHOR(S)

Erkki Ruoslahti

Email: ruoslahti@burnham.org

5d. PROJECT NUMBER

5e. TASK NUMBER

5f. WORK UNIT NUMBER

7. PERFORMING ORGANIZATION NAME(S) AND ADDRESS(ES)

The Burnham Institute
La Jolla, CA 92037

8. PERFORMING ORGANIZATION REPORT NUMBER

9. SPONSORING / MONITORING AGENCY NAME(S) AND ADDRESS(ES)
U.S. Army Medical Research and Materiel Command
Fort Detrick, Maryland 21702-5012

10. SPONSOR/MONITOR'S ACRONYM(S)

11. SPONSOR/MONITOR'S REPORT NUMBER(S)

12. DISTRIBUTION / AVAILABILITY STATEMENT
Approved for Public Release; Distribution Unlimited

13. SUPPLEMENTARY NOTES
Original contains colored plates: ALL DTIC reproductions will be in black and white.

14. ABSTRACT

Anti-angiogenic therapy appears to eliminate immature blood vessels. This paradoxically leads to improvement of tumor blood supply, as the structure and function of mature tumor blood vessels, not specific for anti-angiogenic effect, is normalized. This is a serious limitation to the anti-angiogenic therapy. The goal of this project is to specifically distinguish these "normalized" therapy resistant vessels in breast cancer from those sensitive to anti-angiogenic treatment. To achieve this, we have developed tumor models for vascular normalization and are using *in vivo* phage display and isolation of peptides that specifically home to normalized tumor vessels resistant to anti-angiogenic therapy. The results obtained in this study will enable specific targeting and thus treatment of breast cancer vessels not responding to standard anti-angiogenic therapy.

15. SUBJECT TERMS
anti-angiogenesis, phage display, tumor homing peptides

16. SECURITY CLASSIFICATION OF:			17. LIMITATION OF ABSTRACT	18. NUMBER OF PAGES	19a. NAME OF RESPONSIBLE PERSON
a. REPORT	b. ABSTRACT	c. THIS PAGE			USAMRMC
U	U	U	UU	35	19b. TELEPHONE NUMBER *(include area code)*

This report contains unpublished results.
This information is privileged and confidential.

DOD W81 XWH-06-1-0482
Targeting Therapy-Resistant Tumor Vessels

PI: Erkki I. Ruoslahti, M.D., Ph.D.

FRONT COVER

REPORT DOCUMENTATION PAGE

TABLE OF CONTENTS

This report contains unpublished results.
This information is privileged and confidential.

1. INTRODUCTION

The overall goal of this project is to identify peptides that selectively recognize breast cancer vessels that remain after anti-angiogenic treatment. Like all other tissues, cancerous tumors need a blood supply. To obtain blood supply, a tumor stimulates the growth of new blood vessels in a process known as angiogenesis. Preventing tumor angiogenesis has become a promising new form of cancer therapy, including that of breast cancer. However, researchers have found that such therapy preferentially destroys the immature tumor vessels, and leaves behind the more established vessels. These remaining vessels can keep providing the tumor with a blood supply. We are using *in vivo* phage display to target vessels that remain after anti-angiogenic therapy. Markers of such vessels will be useful in developing strategies for complete destruction of breast cancer vasculature, and in assessing the potential of anti-angiogenic therapy in individual patients.

2. PROGRESS REPORT

Task 1. To develop two tumor models for anti-angiogenic therapy and subsequent phage library screening.

We have shown that anti-nucleolin treatment of mice with 4T1 tumors reduces blood vessel density within the tumors and have characterized the vessel normalization in detail using MDA-MD-435 tumors. Data presented in the Appendix provide additional data supportive of the normalization of tumor vessels as a result of anti-nucleolin treatment. In addition to showing that the vessels remaining after the treatment contain a pericyte coat, we show that vessel architecture is normal, the diameter of the vessels is smaller (dilated, abnormal vessels are gone), a basement membrane is present, and tumor hypoxia is reduced. Thus, this model is clearly suitable for the phage screening we proposed.

We are in the process of making arrangements to obtain the second model, anti-VEGF-treated tumors. We are in negotiations with a company (under a confidentiality agreement) that has a VEGF system inhibitory antibody intended for clinical use. The goal is to have them provide us with the antibody and/or tumor mice that have been treated with the antibody. The agreement is in place at the scientist level, but the legal/administrative review at the company has been slow. We are keen on using this system because it is clinically highly relevant.

Task 2. To screen phage libraries for peptides that specifically recognize vessels in tumors treated with anti-angiogenic therapy.

This report contains unpublished results.
This information is privileged and confidential.

The screenings have been initiated. We have performed one round of *in vivo* screening using tumor mice treated with anti-nucleolin and expect to complete the next several rounds within the next month or two.

We have also devised a new *ex vivo* screening protocol in which we can use tumor mice that have not been treated with anti-angiogenic agents. We inject the mice with a phage library, perfuse the mouse to remove phage remaining in the circulation, collect the tumor, and isolate endothelial cells using a CD31 antibody. We have used this procedure in our earlier phage work (e.g. Zhang et al., 2006). The new twist is that we will next remove those endothelial cells that come from the poorly developed (angiogenic) vessels, and then rescue the phage that has bound to (or become internalized by) the well-formed (mature) blood vessels that would have remained as a result of blood vessel normalization. We use anti-nucleolin to remove the endothelial cells (and phage associated with them) from poorly formed vessels. We also plan to use antibodies against integrin subunits $\alpha 5$ and αv because a recent paper shows that the $\alpha 5\beta 1$ and $\alpha v\beta 3$ integrins, which are highly expressed in tumor vessels, are lost as a result of anti-angiogenic treatment (Yao et al. 2006). This procedure shifts the antibody treatment *in vitro,* and we expect it to greatly speed up and simplify the peptide identification.

Task 3. To validate the specificity of the peptides isolated in the screening

We have not come to this stage yet.

3. KEY RESEARCH ACCOMPLISHMENTS

We have worked on establishing the tumor systems for the screening and initiated the phage screening. The screening work is still in its early stages, so there are no peptide sequences to report at this time. Our results regarding the effect of anti-nucleolin on MDA-MD-435 tumor vasculature are of interest (Appendix) because we see striking vessel normalization without any effect on tumor growth. In previous studies, vessel normalization has been associated with reduced tumor size. We are working on a few remaining experiments to complete the story and publish it.

4. REPORTABLE OUTCOMES

We have helped Dr. Pirjo Laakkonen (a former postdoc) in Helsinki with a project that relates to the theme of this grant. She has used *in vivo* phage screening to identify a peptide that recognizes co-opted blood vessels in a glioma model. A patent

application, in which the Burnham Institute will be one of the assignees, is being prepared on this peptide.

5. CONCLUSIONS

We are making good progress according to the SOW. The tumor models for vascular normalization have been established, and the phage screening has been initiated. We expect to publish the tumor model data.

6. REFERENCES

Zhang, L. Giraudo, E., Hoffman, J.A., Hanahan, D. and Ruoslahti, E. Lymphatic zip codes in premalignant lesions and tumors. *Cancer Res.* 66: 5696-5706 (2006).

Yao, V.J., Ozawa, M.G., Varner, A.S., Kasman, I.M., Chanthery, Y.H., Pasqualini, R., Arap, W. and McDonald, DM. Antiangiogenic therapy decreases integrin expression in normalized tumor blood vessels. *Cancer Res.* 66:2639-2649 (2006).

7. APPENDIX

See Attached

Rabbit IgG treatment

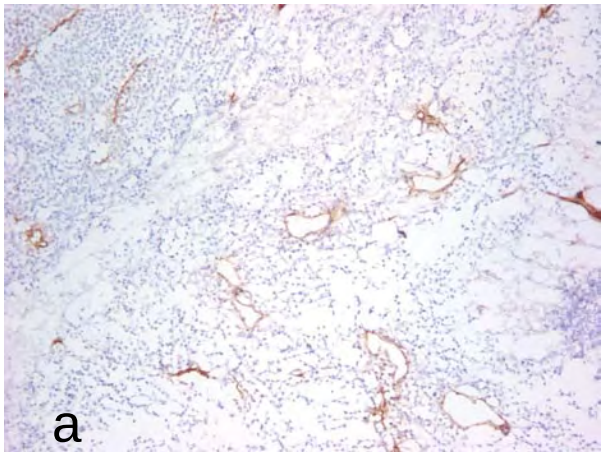

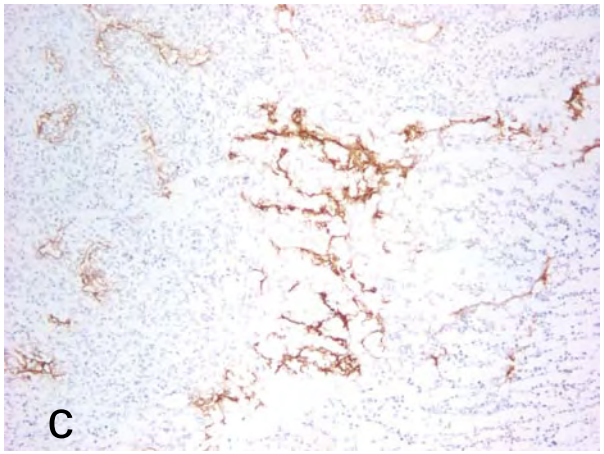

NCL3 treatment

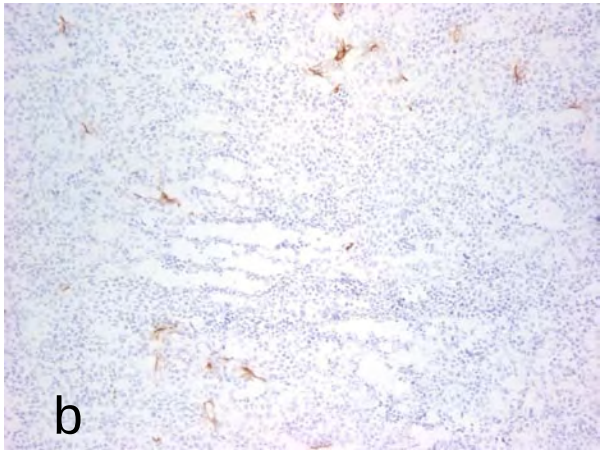

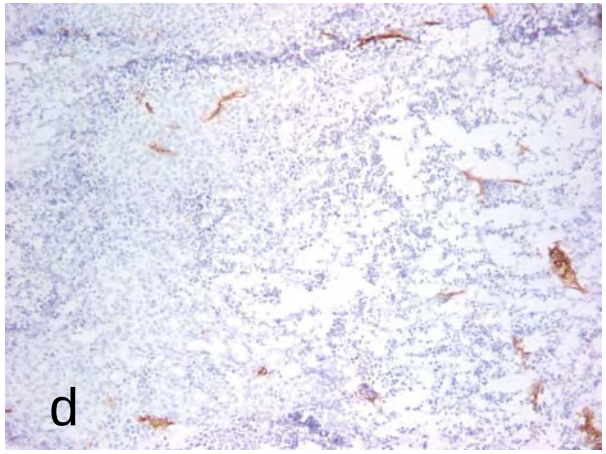

Anti-nucleolin antibody NCL3 normalizes the architecture of the tumor vasculature. Mice bearing MDA-MB-435 tumor xenografts were treated for 4 weeks as described before. Immunostaining of CD31 was used to analyze the architecture of tumor vasculature. Tumor vessel diameters in control (a) and NCL3 treated tumors (b). (c-d) NCL3 treatment reduces tumor vessel tortuosity. (c) Control, (d) NCL3 treated.

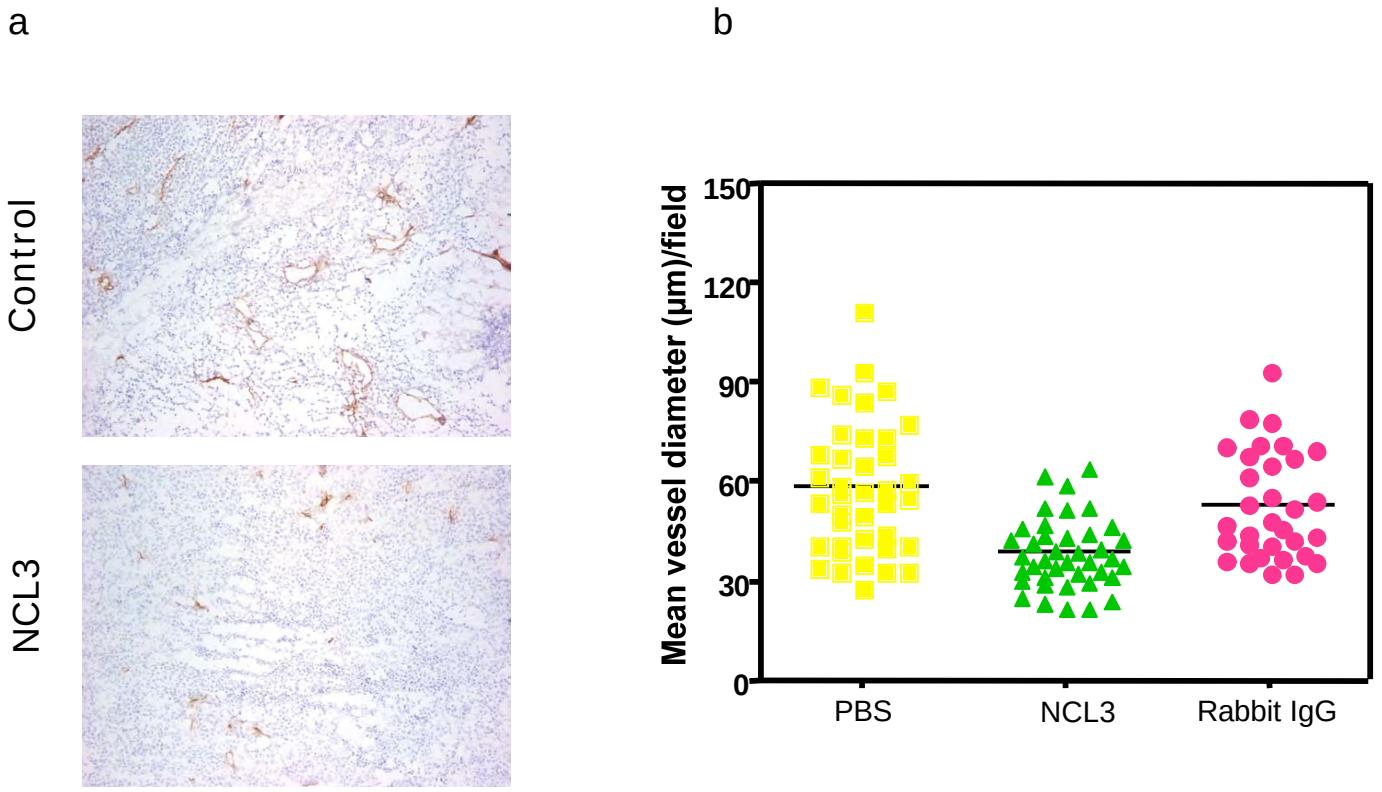

Anti-nucleolin treatment reduces vascular diameter. (a) CD31 staining in control (PBS or rabbit IgG N=5 per group) and NCL3 treated (N=5) tumors. (b) Diameter of DC31 positive vessels in control and NCL3 treated animals. Each data point represents the mean vessel diameter obtained from the quantification of 8 vessel areas per tumor ($p<0.001$).

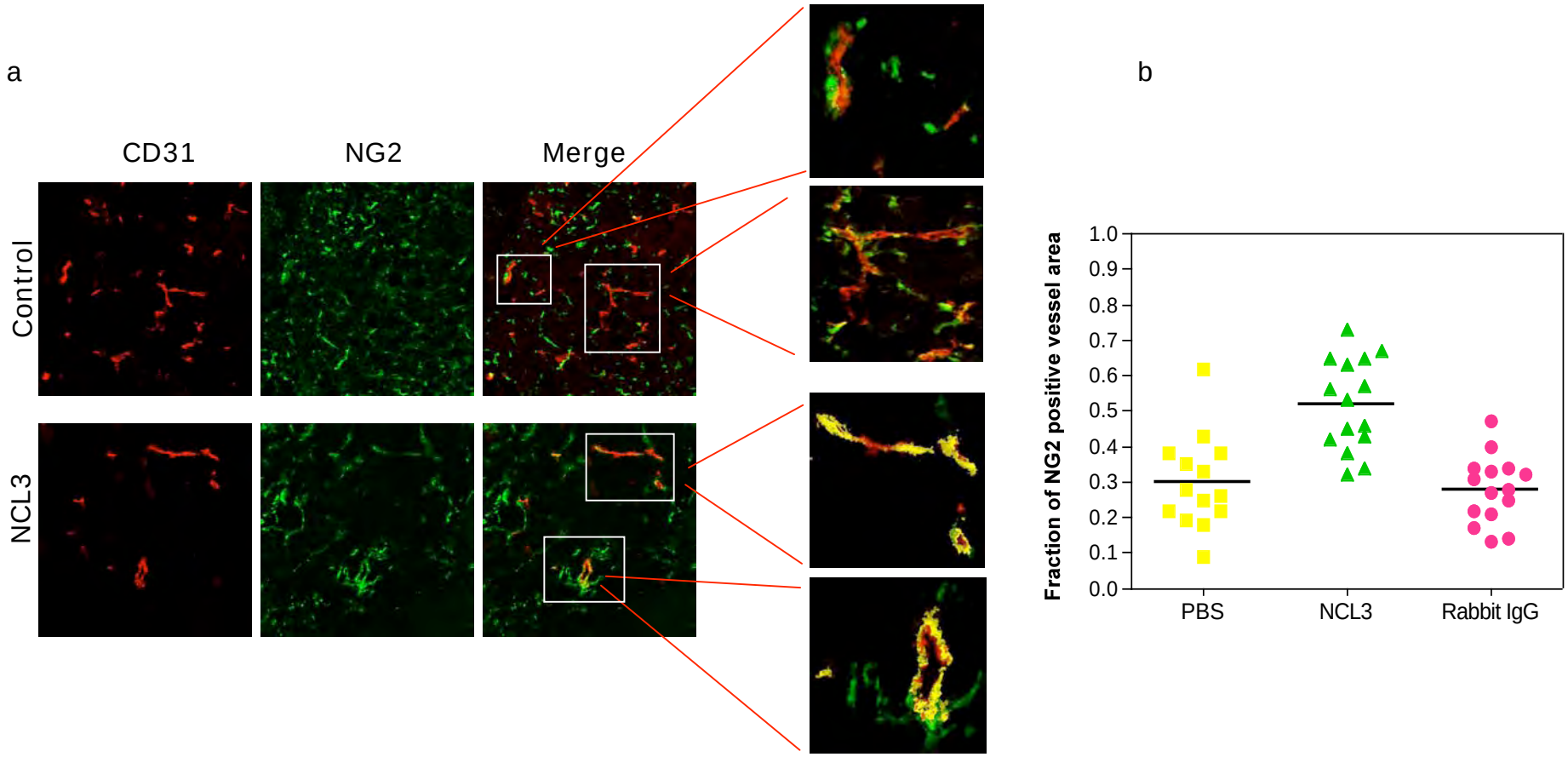

Anti-nucleolin treatment increases pericyte coverage of non-regressed tumor vessels. Tumor sections of control and NCL3 treated tumors were co-stained for CD31 and NG2. Confocal image stacks (20-30 slices per stack) of three well-vascularized tumor regions were obtained (N=5 tumors per group) and subsequently converted to 3D images by Volocity software for quantification of pericyte (NG2) coverage. (a) The large images on the left are maximum intensity projections (obtained by Image J software) of representative tumor regions in control and NCL3 treated animals as indicated. The enlarged frames are the 3D rendering images of representative blood vessels, which were used for the quantification reported in (b). The areas of overlap between NG2 and CD31 signals, calculated by the Volocity software, are indicated in yellow. Each data point in (b) represents the mean NG2 coverage per vessel areas analyzed ($p<0.001$).

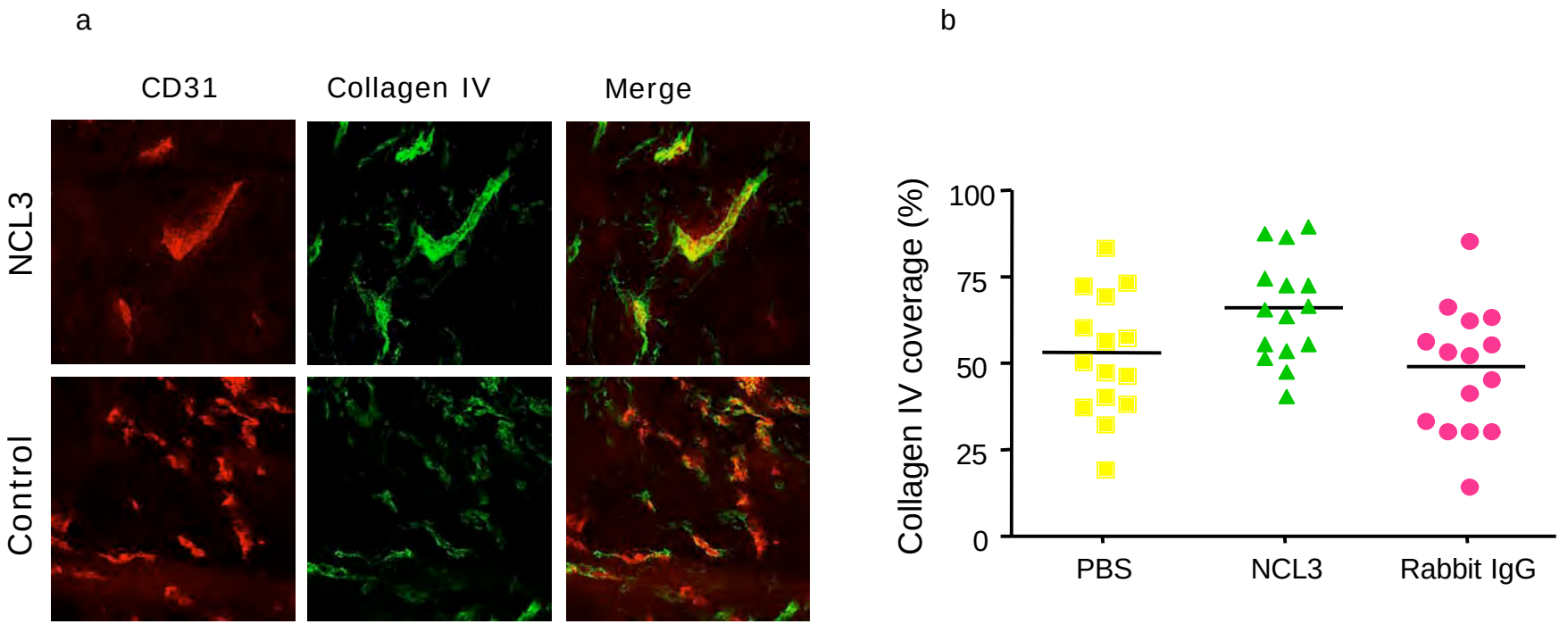

Anti-nucleolin treatment increases the fractional coverage of vascular endothelium by the basement membrane. (a) Histological sections of tumors from control (PBS or rabbit IgG, N=5 per group) and NCL3 (N=5) treated animals were stained with CD31 and collagen IV specific antibodies. Confocal images of three well vascularized areas per section, were taken and converted into 3D images by Volocity software for quantification of collagen IV coverage (b). Each data point represents the mean of collagen IV coverage per vessel area analyzed ($p<0.03$).

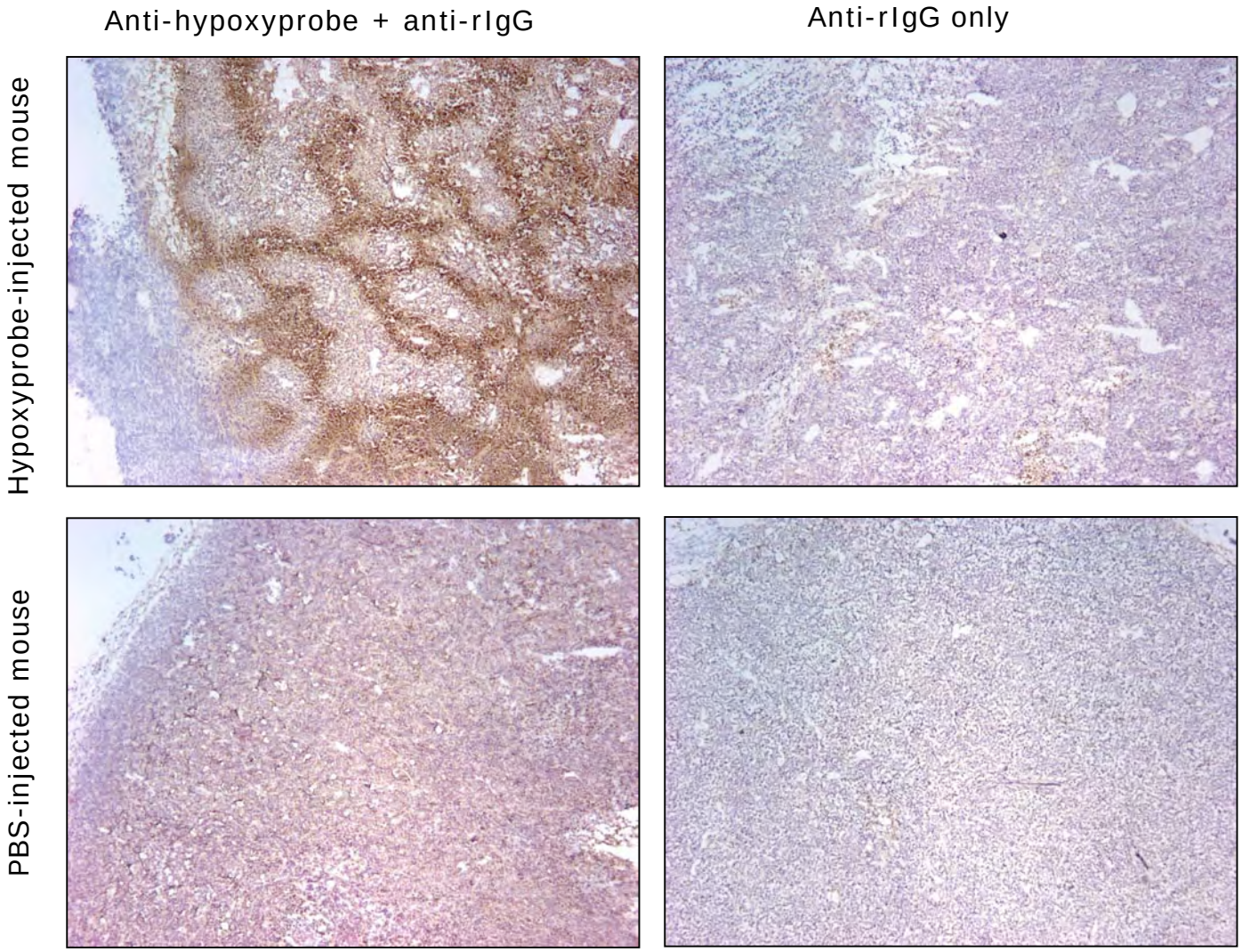

Detection of hypoxia in MDA-MB-435 tumor xenografts and antibody controls. MDA-MB-435 tumor bearing mice were i.v. injected with either PBS or 60mg/kg (mice body weight) of hypoxyprobe (pimonidazole hydrochloride) in PBS and sacrified 1h post injection by perfusion through the heart with PBS. Hypoxic areas were detected on tumors frozen sections by immunohistochemistry with FITC conjugated anti hypoxiprobe primary antibody and anti FITC-HRP conjugated secondary antibody (II Ab). The specificity of hypoxic areas staining was confirmed by staining with secondary Ab only and staining on tumor sections from mice injected with PBS only.

a

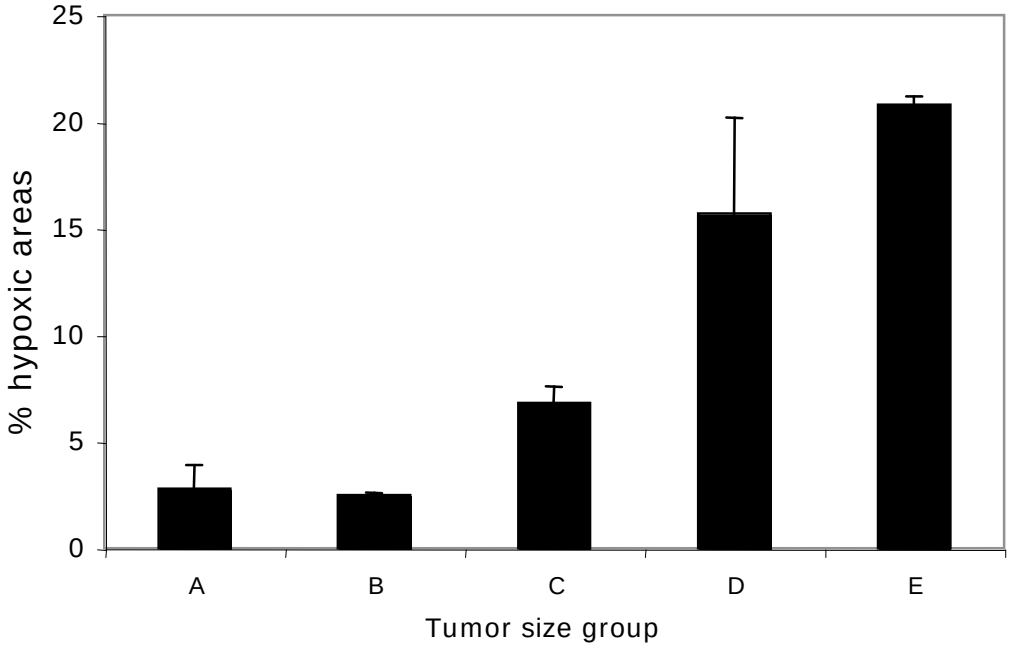

Group tumor size	d (mm)	D (mm)
A	3.4±0.15	3.5±0.2
B	5.3±0.17	7±0.26
C	5.7±0.74	7.9±0.12
D	8.2±0.21	9.1±0.35
E	9.4±2.25	13.3±1.15

b

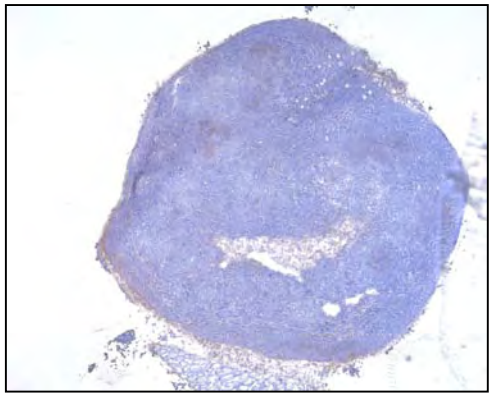

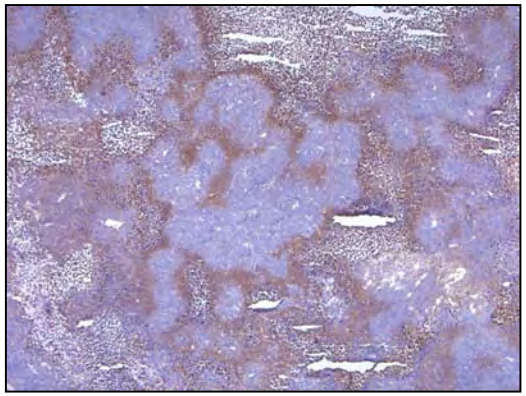

Detection of hypoxia at different stages of tumor growth. Mice bearing MDA-MB-435 tumor xenografts of different size were i.v. injected with either PBS or 60mg/kg of hypoxyprobe and sacrified 1h post injection by perfusion through the heart with PBS. Hypoxic areas were detected on tumor frozen sections by immunohistochemistry of hypoxiprobe and quantified by an algorithm computer program (a-left panel). Each tumor size group was defined by the smallest (d) and largest (D) diameter of the tumor (a-table on the right). (b) Representative hypoxia staining in tumors of size belonging to group A and E. N=3 mice/group.

a

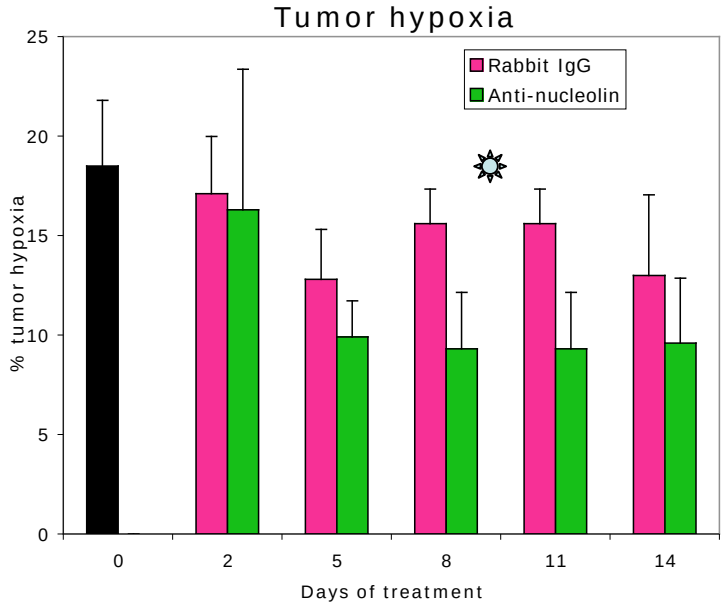

b

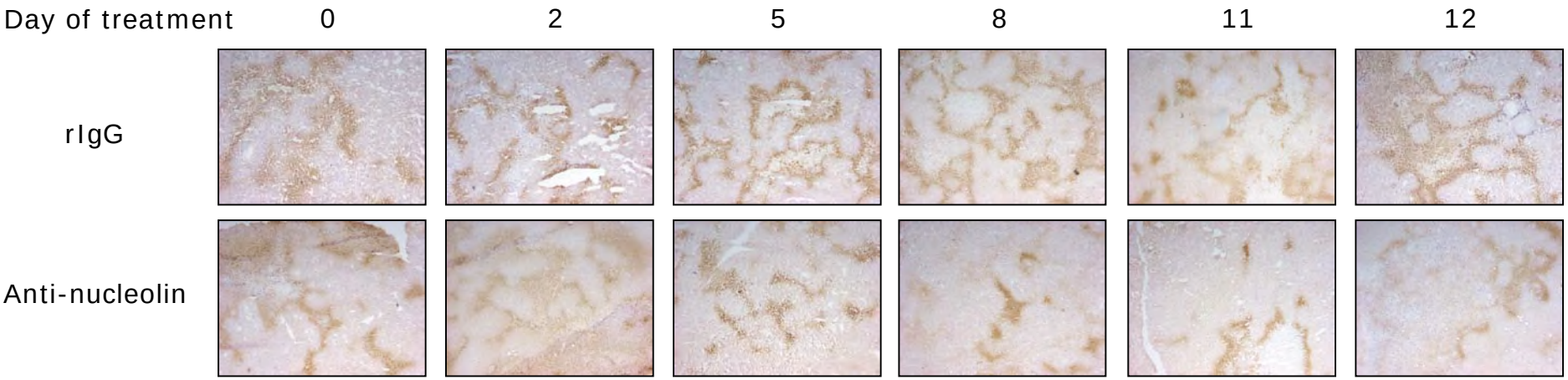

Anti-nucleolin treatment reduces tumor hypoxia. MDA-MB-435 tumor bearing mice were iv injected every three days with 250µg of either NCL3 antibody or rabbit IgG as a control.During a 14-day time frame, tumor hypoxia remains relative constant in control mice, but decreases after 8 days of treatment with anti-nucleolin antibody ($p<0.05$). To measure tumor hypoxia pimonidazole hydrochloride (hypoxyprobe-1) was iv injected 1h before the tumor was rapidly frozen. An antibody against pimonidazole-protein adducts was used to detect hypoxic regions in tumor sections (a). Hypoxic areas were measured with an algorithm computer program (a).

Lymphatic Zip Codes in Premalignant Lesions and Tumors

Lianglin Zhang,[1] Enrico Giraudo,[4] Jason A. Hoffman,[2,3] Douglas Hanahan,[4] and Erkki Ruoslahti[1]

[1]Cancer Research Center and [2]Program in Molecular Pathology, Burnham Institute for Medical Research; [3]Department of Pathology, University of California San Diego, School of Medicine, La Jolla, California; and [4]Department of Biochemistry and Biophysics, and the Diabetes and Comprehensive Cancer Centers, University of California at San Francisco, San Francisco, California

Abstract

Blood vessels in tumors are morphologically and functionally distinct from normal resting blood vessels. We probed lymphatic vessels in premalignant lesions and tumors by *in vivo* screening of phage-displayed peptide libraries, asking whether they too have distinctive signatures. The resulting peptides begin to define such signatures. One peptide identified the lymphatics in a human melanoma xenograft. Another recognized the lymphatics in prostate cancers but not in premalignant prostate lesions; this peptide similarly identifies human prostate cancer lymphatics. A third was selective for the lymphatics in the premalignant prostate lesions. A fourth identified the lymphatics in dysplasias and squamous carcinomas of the cervix and skin. None recognize lymphatics in normal tissues. Thus, tumor development is associated with organ- and stage-specific changes in lymphatics. Systemic treatment of mice with fusions of a lymphatic homing peptide and a proapoptotic motif reduced the number of tumor lymphatics in prostate tumor and melanoma, forecasting future lymphatic targeting agents for detection and therapeutic intervention. (Cancer Res 2006; 66(11): 5696-706)

Introduction

The endothelial lining of blood vessels is highly diversified. Many, and perhaps all, normal tissues impart a tissue-specific "signature" on their vasculature, and tumor vessels differ from normal vessels both in morphology and molecular composition (1). Tumors induce angiogenesis to support expansive growth (2) and many of the changes in tumor vessels are angiogenesis related (3–6). Moreover, tumor blood vessels have tumor type–specific and, in some stages, stage-specific characteristics; *in vivo* screening of phage libraries has yielded distinct sets of homing peptides selectively recognizing angiogenic signatures in two transgenic mouse models of organ-specific tumorigenesis. Homing peptides can also distinguish the angiogenic blood vessels of premalignant lesions from those of fully malignant lesions in the same tumor model (7, 8), indicating that vascular changes mirror the stage of tumor development.

The lymphatic system constitutes a second vascular system, one that has only an efferent arm. Tumors frequently induce lymphangiogenesis, as well as co-opt existing lymphatics (9–11). Tumors may contain intratumoral lymphatics, but, more commonly, an extensive network of lymphatic vessels is present around tumor tissue (12–14). The lymphatics within tumors, when present, are generally nonfunctional in fluid transport (14), possibly reflecting compression by interstitial pressure and blockage by intraluminal tumor cells. The lymphatic vessels in and around tumors are an important conduit of metastasis. Indeed, growth factor–stimulated enhancement of lymphatic vessel expression in tumors increases metastasis (15, 16). Conversely, inhibiting lymphangigenesis suppresses lymphatic metastasis, but generally does not affect tumor growth (17).

A peptide that selectively binds to the endothelial cells of lymphatics associated with a xenotransplanted human breast tumor has been described (13). This was the first demonstration that tumor lymphatics can differ from normal lymphatics, but the larger question of whether tumor lymphatics are generally distinguishable from normal lymphatics has been unanswered.

Here, we identify homing peptides that specifically recognize tumor lymphatics or lymphatics in premalignant lesions in a set of distinctive organ-specific tumor models in mice. Our results show that tumor lymphatics, like tumor blood vessels, express specific markers, and that these lymphatic markers are tumor type specific and distinct from blood vessel markers in the same tumors. The tumor-specific lymphatic vessel markers may be useful in early detection and tumor targeting.

Materials and Methods

Cell Lines, Mice, and Tumors

The following cell lines were maintained in DMEM supplemented with 10% FCS: C8161 human melanoma, MDA-MB-435 human breast cancer, KRIB human osteosarcoma, and human prostate cancer cells PPC1 and DU145. LNCaP human prostate cancer cell line was grown in RPMI 1640 with 10 mmol/L HEPES, 1 mmol/L sodium pyruvate, and 1.5 g/L sodium bicarbonate supplemented with 10% FCS. M12 human prostate cancer cell line was cultured in RPMI 1640 with 5 μg/mL insulin-transferrin-sodium selenite, 2.5 μg/mL fungizone, 50 μg/mL gentamicin, 0.2 μmol/L dexamethasone, 10 ng/mL epidermal growth factor, and 5% FCS (18). To produce tumors, nude BALB/c and C56BL/6 mice were s.c. (C8161, KRIB, and PPC1) or orthotopically (MDA-MB-453, PPC1, DU145, M12, and LNCaP) injected with 1×10^6 tumor cells. Transgenic mouse tumor models included transgenic adenocarcinoma of the mouse prostate (TRAMP), mouse mammary tumor virus (MMTV)-PyMT breast cancer, and K14-HPV16 cervical cancer. To initiate cervical carcinogenesis, female K14-HPV16 mice (19) were treated with 17β-estradiol (E_2; refs. 20, 21). Briefly, 1-month-old virgin female transgenic (heterozygous K14-HPV16, 1203#1) and nontransgenic (FVB/n) mice were anesthetized with isoflurane, and continuous release pellets that deliver E_2 at doses of 0.05 mg over 60 days (Innovative

Note: Supplementary data for this article are available at Cancer Research Online (http://cancerres.aacrjournals.org/).

Current address for E. Giraudo: Division of Molecular Angiogenesis, Institute for Cancer Research and Treatment and Department of Oncological Sciences, University of Turin, 10060 Candiolo, Turin, Italy. Current address for J.A. Hoffman: Genomics Institute of the Novartis Research Foundation, San Diego, CA 92021. D. Hanahan is an American Cancer Society Research Professor.

Requests for reprints: Erkki Ruoslahti, Cancer Research Center, Burnham Institute for Medical Research, 10901 North Torrey Pines Road, La Jolla, CA 92037. Phone: 619-455-6480; Fax: 858-646-3198; E-mail: ruoslahti@ljcrf.edu or Douglas Hanahan, Department of Pathology, University of California San Diego, School of Medicine, La Jolla, CA 92093. E-mail: dh@biochem.ucsf.edu.

doi:10.1158/0008-5472.CAN-05-3876

Research of America, Sarasota, FL) were implanted s.c. in the dorsal back skin. Subsequent pellets were implanted at 3 and 5 months of age for a total of 6 months of hormone treatment. K14-HPV16 mice were maintained in the FVB/n background (FVB/n; The Jackson Laboratory, Bar Harbor, ME). The mice were maintained in accordance with the University of California, San Francisco, institutional guidelines governing the care of laboratory mice. The animal experimentation was approved by Animal Research Committees at University of California, San Francisco, or Burnham Institute for Medical Research.

Phage Library and Screening

A NNK-encoded CX7C library display on T7Select415-1 phage (Novagen, Madison, WI) was prepared as previously described (13). Phage selection and validation have been described (22). A two-step procedure was designed for the selection of peptides targeting the tumor lymphatic vessels of premalignant prostate lesions and prostate tumor. First, the phage library was incubated with cells derived from normal prostate to subtract the phage that bind to normal prostate. Second, the antipodoplanin magnetic beads were used to isolate lymphatic endothelial cells. We did two to three rounds of *ex vivo* selection and two to three rounds of *in vivo* selections.

For the *ex vivo* selections, cell suspensions were prepared from normal prostates of tumor-free littermates of TRAMP mice, premalignant prostates of 14- to 16-week-old TRAMP mice, and tumor tissues of 25- to 28-week-old TRAMP mice. The C57BL6 TRAMP mice display mild to severe hyperplasia by the time they are 12 weeks of age, and severe hyperplasia has developed by 18 weeks (23, 24). Thus, the premalignant lesions of prostate we used represent a mixture of mild or severe hyperplasia. Collagenase IA (1 mg/mL; Sigma, St. Louis, MO) was used to disperse the tissues. About 1×10^7 normal prostate cells were incubated at 4°C for 3 hours with 5×10^{10} plaque-forming units (pfu) of T7 phage displaying a CX7C peptide library. The samples were centrifuged at 1,200 rpm for 10 minutes; the supernatant (the normal prostate-subtracted phage library) was recovered and then incubated overnight at 4°C with 5×10^7 cells derived from premalignant prostate tissue or prostate tumor. The cells were washed to remove unbound phage, incubated with rat anti-mouse podoplanin for 45 minutes at 4°C, and washed thrice with cold PBS containing 0.5% bovine serum albumin (BSA). Podoplanin-positive cells were then isolated using M450 sheep anti-rat IgG Dynabeads (M450; Dynal, Oslo, Norway). Phage that bound to the podoplanin-positive cell population were rescued and amplified in *Escherichia coli*. *In vivo* phage library screening was done as described (13).

Homing Specificity of Phage

In vivo homing specificity of phage was tested as described (22). Briefly, mice bearing tumors were anesthetized and i.v. injected with 5×10^9 pfu phage. After 7 minutes, the mice were perfused through the heart with PBS containing 0.5% BSA. The tumor and control organs were dissected from each mouse and the phage were rescued and tittered. For histology analysis, the mice were perfused with 4% PFA 30 minutes after the injection of phage. Tissues were embedded in Tissue-Tek OCT (Tissue-Tek, Elkhart, IN) and 5 μm sections were prepared for phage immunostaining.

Antibodies and Immunohistology

Custom immunization to produce a rabbit antiserum against mouse Prox-1 was done by Proteintech, Inc. New Zealand White rabbits were immunized with a fusion protein of glutathione *S*-transferase (GST)–COOH-terminal fragment of Prox-1 protein. The antibody was affinity purified on the fusion protein and absorbed with GST. The resulting antibody preparation (1.8 mg/mL) gave a titer of 1:10,000 against the fusion protein in ELISA. Immunofluorescence staining of tissue sections with the anti-Prox-1 antibody gave a pattern of nuclear staining. Antibodies against the lymphatic markers anti-LYVE-1 (13) and antipodoplanin (kindly provided by T. Petrova and K. Alitalo), rat monoclonal anti-mouse CD31 (BD PharMingen, San Diego, CA), rat anti-mouse MECA-32 (BD PharMingen), rabbit polyclonal anti-T7 phage, rabbit anti-mouse cleaved caspase-3 (ASP175; Cell Signaling Technology, Danvers, MA), and rat anti-mouse vascular endothelial growth factor receptor 3 (VEGFR3; provided by H. Kubo and K. Alitalo) were used for immunohistochemical staining of frozen tissue sections as described (8, 13).

The corresponding secondary antibodies were added and incubated for 1 hour at room temperature: AlexaFluor-488 goat anti-rat or rabbit IgG (1:1,000; Molecular Probes, Eugene, OR), AlexaFluor-594 goat anti-rat or rabbit IgG (1:1,000; Molecular Probes), AlexaFluor-594 donkey anti-mouse or goat IgG (1:1,000; Molecular Probes), and AlexaFluor-488 donkey anti-mouse or goat IgG (1:1,000; Molecular Probes). The slides were washed thrice with PBS and mounted in Vectashield Mounting Medium with 4′,6-diamidino-2-phenylindole (DAPI; Vector Laboratories, Burlingame, CA). Blood vessels were also visualized by i.v. injecting *Lycopersicon esculentum* (tomato) lectin conjugated to fluorescein (100 μg of lectin in 200 μL PBS; Vector Laboratories).

Tissue distribution of fluorescein-labeled peptides (25) was studied by i.v. injecting the peptide (100-150 μg in 200 μL PBS) into the mice. The injected peptides were allowed to circulate 30 minutes to 2 hours, and the mice were perfused with 4% paraformaldehyde through the left ventricle of heart. Tissues were dissected and frozen in OCT embedding medium (Tissue-Tek). The frozen sections were prepared for immunohistologic analysis.

Peptide Synthesis

Peptides were synthesized in our peptide facility using Fmoc chemistry in a solid-phase synthesizer. The peptides were purified by high-performance liquid chromatography and confirmed by mass spectrometry. Fluorescein-conjugated peptides were synthesized as described (25). The LSD and REA peptides were synthesized as the chimera with the proapoptotic motif $_D$(KLAKLAK)$_2$ (26).

Targeted Proapoptotic Peptide Treatment of Tumor-bearing Mice

Prostate cancer model. Orthotopic xenografted prostate tumors were established by injecting 1×10^6 PPC1 human prostate cancer cells into the mouse prostate. Fifteen days postinoculation, the mice were i.v. injected with $_D$(KLAKLAK)$_2$-CREAGRKAC, an equimolar mixture of $_D$(KLAKLAK)$_2$ and CREAGRKAC, or PBS. Mice were given 200 μg of the conjugate per week divided into two injections (26, 27).

Melanoma model. Nude BALB/c mice were s.c. injected with 1×10^6 C8161 human melanoma cells. Treatment started when mean tumor volumes reached ~100 mm^3. Mice with size-matched tumors were randomized into three groups. The therapeutic group received a chimera of tumor-homing peptide with the proapoptotic motif [$_D$(KLAKLAK)$_2$-CLSDCGKRKC]. The control groups received an equimolar mixture of CLSDGKRKC and $_D$(KLAKLAK)$_2$, or PBS alone. The tumor-bearing mice were i.v. injected with 200 μg/dose/mouse weekly for 3 weeks (26, 27).

The mice were monitored for weight loss, and tumors were dissected and weighed at the termination of the experiment. Histologic analysis was done to evaluate the density of tumor lymphatics and blood vessels. Apoptotic lymphatic endothelial cells were visualized by double staining with anticleaved caspase-3 and antipodoplanin antibodies. The animal experiments reported here were approved by the Animal Research Committee of Burnham Institute for Medical Research.

Phage Overlay of Tissue Sections From Human Cancer

The frozen sections of human prostate tumor specimens were obtained from Dr. Daniel Mercola (Sidney Kimmel Cancer Center, La Jolla, CA). The sections (5 μm) were preincubated with blocking buffer (5% normal goat serum and 0.5% BSA in 1× PBS) for 1 hour at room temperature, washed thrice with diluted blocking buffer (1:10), and phage (3×10^9 pfu) were incubated on the section for 4 hours. After three washes, rabbit anti-phage antibody (10 μg/mL) was added and the phage incubated for 2 hours. The slides were washed and incubated with AlexaFluor-488 goat anti-rabbit IgG for 1 hour. After further washes, the slides were mounted with Vectashield (Vector Laboratories).

Statistical Analysis

Student's *t* test was used in statistical analysis of the results. The bar diagrams show mean and SD.

Results

Phage targeting of lymphatics in C8161 melanoma. We chose the C8161 human melanoma as the first topic because xenografts of tumors generated with this cell line in nude mice contain lymphatic vessels that are not recognized by the homing peptide LyP-1, which binds to lymphatic endothelial cells in breast carcinomas (13). Our experimental design was aimed to determine whether lymphatic homing peptides having analogous specificity for the melanoma-associated lymphatics could be identified. We modified our earlier protocols to increase the probability of obtaining peptides that recognize tumor lymphatics. We incubated a phage display library with a cell suspension of whole C8161 tumor tissue, allowing phage to bind, and then used immunomagnetic beads to isolate lymphatic endothelial cells that carried along any phage bound to these cells. This enrichment step yielded a phage pool that bound 250-fold more efficiently to the isolated cells than nonrecombinant phage (Supplementary Fig. S1*A*). The enriched phage pool was used in subsequent *in vivo* rounds to select phage that homed to C8161 xenograft tumors. Two rounds of selection *in vivo* produced a 40-fold enrichment of phage (Supplementary Fig. S1*B*). There was no enrichment in the several control organs tested.

The 48 phage clones from the second *in vivo* round of phage pool selection included five clones that appeared most frequently, and these were analyzed further. Two clones displaying peptides with related amino acid sequences (CLSDGKRKC and CLDGGRPKC) bound to cell suspensions prepared from C8161 tumors; the stronger binder, CLSDGKRKC, bound 100-fold more than control phage. I.v. injection of phage into nude mice bearing C8161 tumors showed that both phage homed selectively to the tumors; CLSDGKRKC was about twice as efficient as CLDGGRPKC (the results for CLSDGKRKC are shown in Fig. 1*A*). The CLSDGKRKC peptide (referred to below as LSD) was chosen for further study.

To establish that the homing ability of LSD phage is due to the displayed peptide sequence, we chemically synthesized the peptide as a fluorescein conjugate peptide and i.v. injected the conjugate into C8161 tumor mice. After 2 hours of circulation, the peptide was detected within the tumors (Fig. 1*B*), but not in control organs (Supplementary Fig. S1*C*). Staining of tissue sections with the lymphatic vessel markers podoplanin, Prox-1, LYVE-1, and VEGFR3 showed colocalization of the LSD fluorescence with them (Fig. 1*C*), whereas there was no colocalization with the blood vessel markers MECA-32 and CD31 (Fig. 1*D*). Quantification showed that 85% of the lymphatic vessels that were positive for the peptide were also positive for podoplanin.

We further tested the homing of LSD phage to other types of cancer, including the MDA-MB-435 human breast cancer xenografts recognized by the previously described lymphatic homing peptide, LyP-1 (13). I.v. injected LSD phage did not appreciably home to MDA-MB-435 tumors (see below). These data show that LSD-peptide selectively homes to the lymphatic vessels in C8161 melanoma.

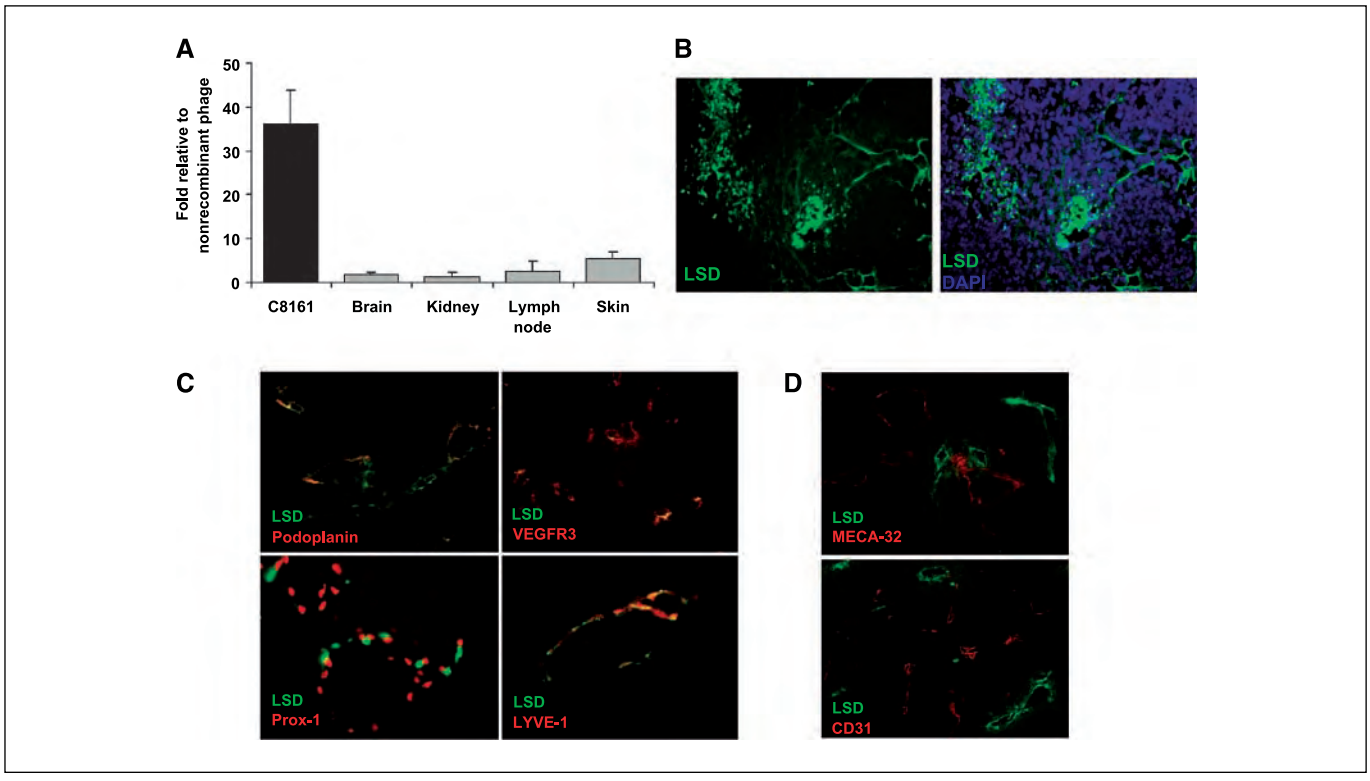

Figure 1. A homing peptide recognizes C8161 melanoma lymphatics. *A,* homing of LSD phage to C8161 xenografts. The LSD phage clone (2×10^9 pfu) was injected i.v. into mice bearing C8161 xenograft tumors and allowed to circulate for 7 minutes. Phage titers recovered from tumors and control tissues are shown. Phage accumulation in C8161 tumor tissue was significantly higher than in normal tissues ($P < 0.03$ relative to the normal tissue with the highest phage uptake, the skin; $n = 3$). *B, in vivo* localization of fluorescein-labeled LSD peptide. The peptide (150 μg) was i.v. injected into C8161 tumor mice, and the tumors and various control tissues were collected for histologic analysis 2 hours after the injection. *Green fluorescence,* presence of the peptide; *blue,* nuclei (DAPI staining). Original magnification, ×200. *C,* colocalization of the LSD peptide with lymphatic markers. The green FITC fluorescence colocalizes with red staining for the lymphatic vessel markers podoplanin, VEGFR3, Prox-1, and LYVE-1 in vessel-like structures within the tumor tissue and at tumor periphery (*bottom left*). *D,* LSD peptide does not colocalize with blood vessel markers. Tumor blood vessels were stained with anti-MECA-32 or anti-CD31 (*red*). Original magnification (*C* and *D*), ×400.

Phage targeting of lymphatics in premalignant lesions and tumors of prostate. Seeking to further generalize the proposition that tumor-associated lymphatics might have organ-specific signatures, we selected lymphatic homing peptides in the TRAMP transgenic mouse model of *de novo* prostate carcinogenesis (28). Immunohistochemical analysis had revealed abundant lymphatics associated both with premalignant lesions and tumors in this model (Supplementary Fig. S2*A*). As it is possible to access premalignant lesions in this system, we also explored the possibility of distinguishing the lymphatics of such lesions from those of fully developed tumors. We studied TRAMP mice inbred into C57BL6, a genetic background wherein prostate tumorigenesis occurs over a 30-week time course to terminal disease, with a discernable premalignant phase ($\sim$10-20 weeks).

To isolate peptides that selectively home to fully developed tumors in the TRAMP model, we first pretreated the phage library with cell suspensions derived from normal prostate to decrease the abundance of phage that bind to normal prostate. The normal prostate-subtracted library was then enriched by two rounds of *ex vivo* selection on lymphatic endothelial cells immunopurified from tumors of 25- to 28-week-old TRAMP mice. Three subsequent *in vivo* selection rounds yielded a phage pool that showed nearly 50-fold enrichment for tumor homing. Five peptide sequences were represented more than once in this pool. Three of these phage clones with amino acid sequences CREAGRKAC, CSMSAKKKC, and CKTRVSCGV showed robust binding to tumor-derived cell suspensions and were further tested *in vivo*. I.v. injected CREAGRKAC phage became 50-fold enriched in TRAMP tumors relative to nonrecombinant phage, whereas the other two phage showed $\sim$30-fold enrichment. We chose the CREAGRKAC (REA) for further study.

To screen for peptides recognizing the premalignant lymphatics, we first treated the phage library with cell suspensions derived from normal prostate, and the subtracted library was then enriched on immunopurified lymphatic endothelial cell suspensions derived from prostates containing premalignant lesions, the so-called prostatic intraepithelial neoplasia, or PIN (in 14- to 16-week-old mice). The sequential *ex vivo* selections yielded a phage pool that was 60-fold enriched for binding to the target cells, and a 30-fold enrichment for homing to prostate with PIN lesions was obtained in a subsequent *in vivo* selection. Five phage clones were chosen for evaluation of *in vivo* homing based on their frequent appearance among 64 clones sequenced (32 clones each from the second *ex vivo* round and the third *in vivo* round). Of these, three clones with amino acid sequences CAGRRSAYC, CASLSCR, and CSGGKVLDC, bound to cell suspension derived from PIN lesions (data not shown). These candidates were further tested *in vivo* individually. Phage-displayed peptides CAGRRSAYC, CSGGKVLDC, and CASLSCR showed 24-, 14-, and 12-fold enrichment to PIN lesions relative to nonrecombinant phage, respectively. The CAGRRSAYC (AGR) was chosen for further study.

To evaluate the specificity of the REA and AGR peptides, we i.v. injected the phage into TRAMP mice with either premalignant PIN lesions or prostate tumors, or into their tumor-free (transgene negative) male littermates with normal prostates. The results showed that the REA phage homes to tumors, but not to PIN lesions or normal prostate, whereas the AGR phage homes only to PIN (Fig. 2*A*). Neither phage was found in other tissues, including lymph nodes, kidneys, lungs, skin, or intestine, at levels higher than the nonrecombinant control phage.

In vivo distribution of fluorescein-conjugated REA and AGR peptides after i.v. injection confirmed the phage results. The REA peptide accumulated in prostate tumors, showing 90% overlap with podoplanin-positive lymphatic vessels, whereas PIN lesions, normal prostate (Fig. 2*B*), and control organs (Supplementary Fig. S2*B*) were negative. The AGR peptide selectively homed to PIN lesions, but little or no peptide was seen in prostate tumors, normal prostate tissue (Fig. 2*B*), or in control tissues (Supplementary Fig. S2*C*).

To study the association of REA and AGR peptides with the vasculature, the phage or fluorescein-labeled peptides were i.v. injected into TRAMP mice and phage and peptide localization was compared with lymphatic and blood vessel markers localized with antibodies. The phage and their cognate peptides each showed substantial colocalization with the lymphatic markers podoplanin, VEGFR3, LYVE-1, and Prox-1 in their respective lesions, whereas their localization was entirely distinct from that of the blood vessel markers CD31 and MECA-32. The overlap of the peptides with Prox-1 was less obvious than with the other markers, presumably because Prox-1 is nuclear, whereas the peptides associate with the cell membrane. The results for the REA and AGR peptides are shown in Fig. 2*C* and *D*, and for the REA phage in Supplementary Fig. S2*D*.

Homing peptide for lymphatic vessels in cervical cancer. In a previous study from our laboratories, we identified a homing peptide for dysplastic skin lesions in K14-HPV16 transgenic mice, which develop skin cancers (7). This peptide, CNRRTKAGC, is similar to LyP-1 (CGNKRTRGC), which selectively recognizes lymphatic vessels and tumor cells in breast cancers (13). Because of this similarity, we asked whether the CNRRTKAGC peptide (LyP-2) also recognizes tumor lymphatics. We tested the LyP-1 and LyP-2 peptides in skin and cervical cancers of the K14-HPV16 transgenic mice. In addition to spontaneously developing angiogenic dysplasias and then squamous cell carcinomas of the skin (29), female K14-HPV16 mice develop cervical cancers when their normally cyclic estrogen levels are sustained with time release pellets (20). The estrogen-treated females undergo neoplastic progression in the cervix mimicking, that inferred for human cervical carcinogenesis (20, 21, 29). The premalignant cervical lesions (also called cervical intraepithelial neoplasia, CIN) and cervical tumors of these mice contain abundant lymphatic vessels as detected by immunostaining for lymphatic markers (Supplementary Fig. S3*A*).

I.v. injected LyP-2 phage showed robust homing both to the premalignant and malignant lesions in the cervix, but not to normal cervix (Fig. 3*A*). Fluorescein-labeled LyP-2 peptide also accumulated in the cervical lesions, colocalizing with LYVE-1 (Fig. 3*B, top*) and podoplanin (82% overlap; data not shown), but not with MECA-32 (Fig. 3*B, bottom*). Additionally, occasional foci of scattered cells in the stroma were labeled, with some apparent intracellular localization; the identity of these cells is currently unresolved. No peptide accumulation was observed in normal cervix (Fig. 3*B*) or in other control tissues, either in lymphatics or in nonvascular cells (Supplementary Fig. S3*B*). LyP-2 also homed to the lymphatics associated with dysplasias and squamous cell carcinomas of the skin in male and female K14-HPV16 mice, but not to normal skin lymphatics (data not shown).

Specificity of lymphatic homing peptides for different types of tumors. Having isolated phage-displayed peptides that homed to the lymphatics of melanoma, prostate, or cervix (the origin and specificity of these peptides is summarized in Table 1), we asked whether they recognized common determinants of the

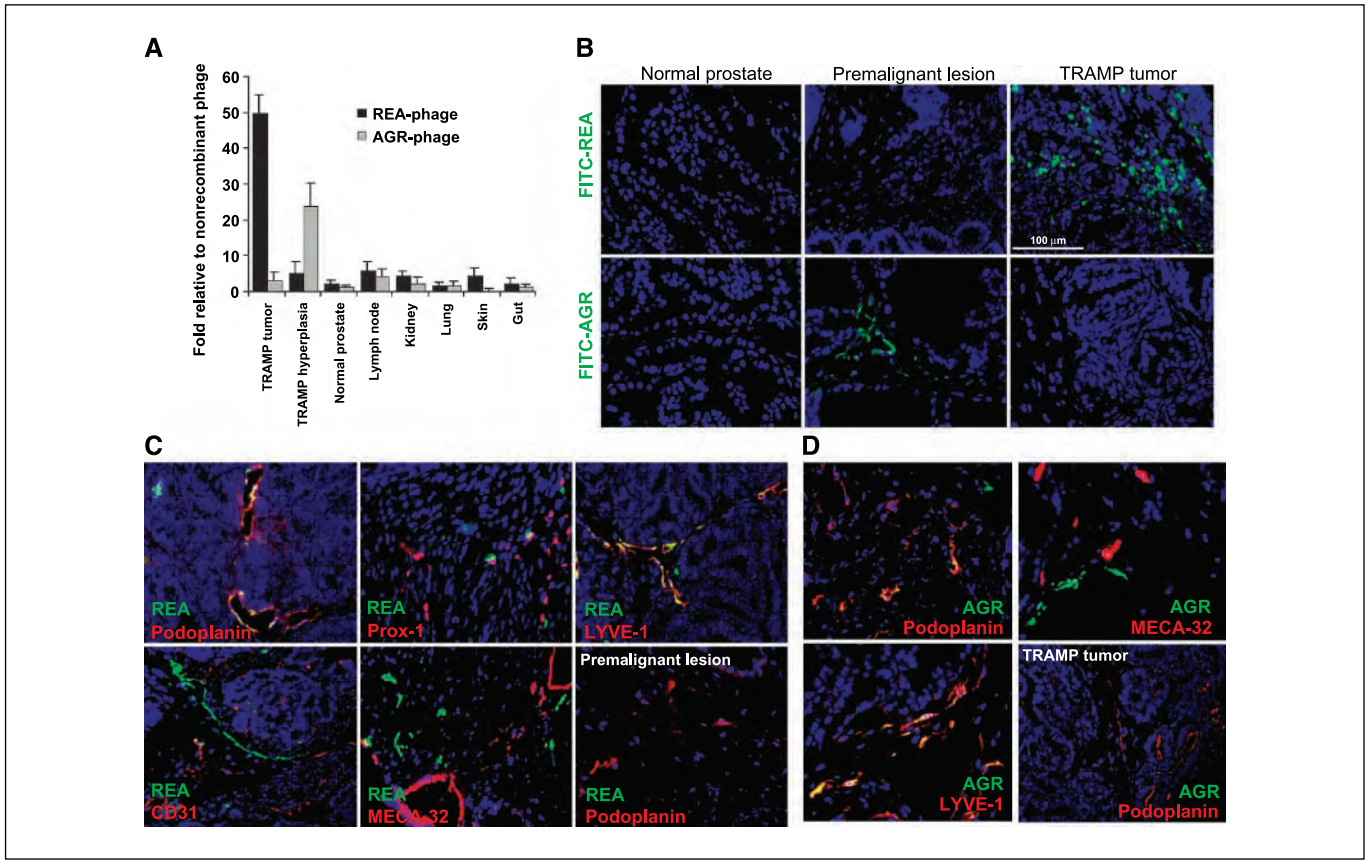

Figure 2. Stage-specific peptides distinguish premalignant lesions and tumors in the prostate of TRAMP mice and colocalize with lymphatic vessels. Phage isolated by screening for homing to TRAMP tumors (REA) or to TRAMP premalignant lesions (AGR) were individually tested in TRAMP mice bearing tumors, or premalignant lesions, and in tumor-free littermates of TRAMP mice with normal prostate. TRAMP mice were i.v. injected with phage or fluorescein-conjugated peptides, and the localization of the phage was studied by phage titration or immunohistochemistry in frozen tissue sections. The peptides were detected in tissue sections by examining fluorescence. The REA phage (*A, black columns*) and peptide (*B, top*) accumulate in TRAMP tumors, whereas the AGR phage (*A, gray columns*) and peptide (*B, bottom*) selectively home to premalignant lesions. The difference between tumor tissue and premalignant tissue was significant for both peptides ($P < 0.01$; $n = 3$-6) Original magnification, ×400. *C,* i.v. injected fluorescein-labeled REA peptide (*green*) colocalizes TRAMP tumor sections with the lymphatic vessel markers podoplanin, Prox-1, and LYVE-1 (*top row*), but not with blood vessel markers (*bottom row*); a premalignant TRAMP lesion does not bind the REA peptide (*bottom row, right*). Original magnification, ×400. *D,* fluorescein-labeled AGR peptide (*green*) colocalizes with podoplanin and LYVE-1 (*red*) in dysplastic prostate lesions, but there is no colocalization with blood vessels detected with MECA-32 staining; a TRAMP tumor does not bind the AGR peptide. Original magnification, ×400.

tumor-associated lymphatic vasculature or organ/tumor selective signatures. The lymphatic homing peptides derived from the different tumor models were tested for their ability to recognize the lymphatics of other tumors. I.v. injected LSD phage did not home to xenotransplant tumors derived from the MDA-MB-435 breast tumor cell line (Fig. 4*A, left*). This phage also did not appreciably home to transgenic mouse tumors of the breast or prostate, or to PPC1 human prostate cancer xenografts; possible low-level homing was seen to squamous carcinomas of the skin in K14-HPV16 mice, and to KRIB human osteosarcoma xenografts. *In vivo* injection of fluorescein-labeled LSD peptide, followed by histologic analysis of peptide distribution, agreed well with the phage results. As shown in Fig. 4*A* (*right*), strong LSD peptide fluorescence was seen in the C8161-derived tumors, the model in which the peptide was selected. The C8161 tumors were positive in nude mice representing two different genetic backgrounds (BALB/c and C57BL/6; shown for the BALB/c strain in Fig. 4*A, right*). In agreement with the phage data, KRIB tumors were weakly positive with the fluorescent peptide, and the other tumors, including the skin cancers, were negative. These results show that the LSD peptide selectively recognizes the lymphatics in the C8161 melanoma–derived tumors.

To profile the homing peptide specificity of the AGR peptide in different types of premalignant lesions, we used three transgenic mouse models, TRAMP, K14-HPV16/E_2, and MMTV-PyMT, which, respectively, develop prostate, cervical, or breast neoplasias that subsequently progress to overt cancer. Both AGR phage (Figs. 2*A* and 4*B*) and fluorescent peptide (Fig. 2*B* and *D*) showed marked preference for the PIN lesions in TRAMP mice; there was little homing of the phage and no detectable homing of the peptide to similar premalignant lesions or malignant tumors in the other two models (Fig. 4*B* and Supplementary Fig. S2*G*).

The REA phage, which was identified in the TRAMP model, also homed to xenografts obtained by orthotopically inoculating into nude mice cells from the human prostate cancer cell lines PPC1, M12, DU145, and LNCaP (Fig. 4*C*). These xenografted tumors were also positive with the fluorescein-conjugated REA peptide (the results for PPC1 are shown in Fig. 4*D*). In contrast, the MDA-MB-435, C8161, and KRIB xenografts, as well as the *de novo* breast and skin cancers arising in MMTV-PyMT or K14-HPV16 mice, respectively, were negative for REA binding (Fig. 4*C* and *D*). The cervical tumors of K14-HPV16/E_2 mice were slightly positive for REA peptide binding, but markedly less so than the prostate tumors. Immunohistochemical analysis showed that FITC-REA

peptide colocalized with lymphatic vessels both within tumor tissues (Fig. 4*D, first row, middle*) and tumor periphery (Fig. 4*D, first row, right*). This was the case with orthotopic prostate tumor xenografts arising from multiple human prostate tumor-derived cell lines (results for PPC1 tumors are shown in Fig. 4*D*). This peptide homed to a lesser extent to K14-HPV16/E_2 cervical tumors (Fig. 4*D*). Interestingly, REA phage homed less efficiently to s.c. xenografts of PPC1 than to orthotopic xenografts of the same tumor cell line (Supplementary Fig. S2*E*). The REA phage strongly bound to PPC1 tumor-derived cell suspensions, but did not bind to cultured PPC1 cells (Supplementary Fig. S2*F*). Thus, REA seems to primarily recognize prostate cancer lymphatics.

We also asked whether the REA peptide recognizes human prostate cancers by using phage overlay of tissue sections. Immunohistochemical staining with antibodies against lymphatic markers Prox-1 and podoplanin revealed abundant lymphatic vessels in human prostate tumors (Fig. 4*D, bottom row, red*). Overlay of tissue sections from two primary human prostate cancers with REA phage indicated that this phage recognizes the lymphatics of human prostate tumors (Fig. 4*D, bottom row, green*). The AGR phage did not bind to the human tumor sections (not shown).

LyP-1 and LyP-2 have different specificities. Given the similar amino acid sequences of the LyP-1 and LyP-2 peptides, and the fact that they both bind to tumor lymphatics, we were interested in comparing their specificities. Surprisingly, these peptides recognize different tumors. Although both peptides homed to the K14-HPV16 skin cancer lymphatics (data not shown), LyP-1 phage homed to MDA-MB-435 breast tumors growing s.c. but not to the *de novo* cervical tumors, whereas the opposite was true of LyP-2 (Fig. 5*A*). Both phage did not home to the normal cervix or normal breast tissue. To confirm these differences in specificity, we coinjected one peptide as a fluorescein conjugate and the other conjugated to rhodamine and vice versa. Both LyP-2 conjugates homed to cervical tumors, whereas neither LyP-1 conjugate did so. The opposite result was obtained when the same conjugates were tested in MDA-MB-435 tumor-bearing mice (Fig. 5*B*). These data indicate that different binding sites exist for the two LyP peptides in different types of tumors.

Lymphatic homing peptide conjugates destroy tumor lymphatics. One potential application of peptides that home and bind to the distinctive lymphatic vasculature of tumors is to target delivery of toxic payloads aiming to disrupt the tumor lymphatics, thereby assessing their functional importance and prospects as a therapeutic target. We began this assessment by linking two of our signature-finding peptides to a toxic agent, assessing its effects on the tumor lymphatics. As a toxic agent, we used conjugates with an apoptosis-inducing peptide, $_D$(KLAKLAK)$_2$. In a previous study,

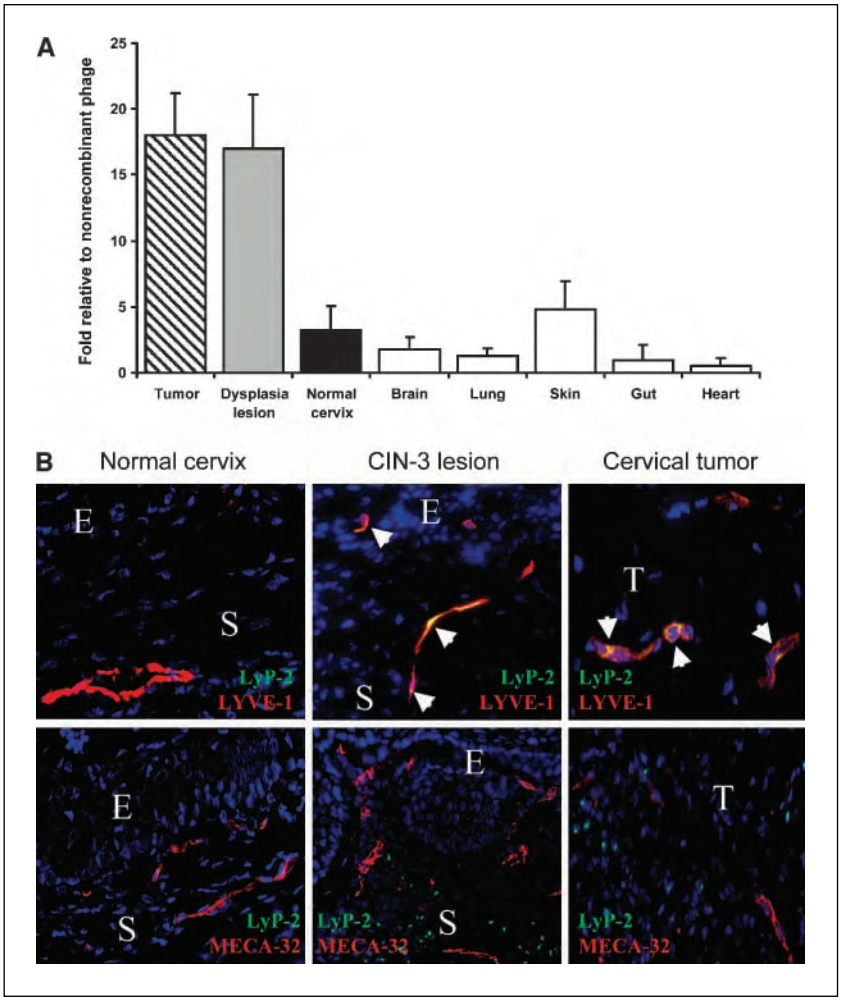

Figure 3. LyP-2 peptide homes to lymphatics in premalignant lesions and tumors of cervix in K14-HPV16/E_2 transgenic mice. *A,* LyP-2 phage (1.5×10^9 pfu) was i.v. injected into mice bearing CIN-3 lesions or tumors of the cervix, and phage titers from the indicated tissues were determined. Significantly more of the LyP-2 phage accumulated in the tumors and dysplastic lesions than in normal cervix ($P < 0.005$; $n = 3$). *B,* FITC-LyP-2 peptide (100 μg) was injected into the tail vein of mice bearing dysplastic lesions or tumors of the cervix and allowed to circulate for 2 hours. FITC-LyP-2 selectively localized within premalignant lesions and tumors, colocalizing with lymphatic vessel markers (shown for LYVE-1; *top row*), but not with the blood vessel markers (shown for MECA-32; *bottom row*). Original magnifications, ×400 (*top*) and ×200 (*bottom*).

this peptide was linked to blood vascular tumor-homing peptides and shown to be selectively cytotoxic to angiogenenic endothelial cells and to have demonstrable antitumor activity (26). To determine whether peptides recognizing tumor lymphatics could be used to target those lymphatics, we synthesized the REA and LSD peptides as conjugates with $_D(KLAKLAK)_2$ and systemically treated mice bearing PPC1 or C8161 xenografts.

Treatment with the REA conjugate had no effect on tumor blood vessel density in the PPC1 tumors, but significantly reduced the number of tumor lymphatics; the uncoupled mixture had no effect on the lymphatics compared with the PBS control (Fig. 6*A*). The conjugate had no effect on tumor growth (Fig. 6*B*), indicating (perhaps not surprisingly) that the tumor-associated lymphatics were not essential for primary tumor growth. Examination of lymphatics in normal skin revealed no discernible effect by the REA or LSD conjugates, and no significant differences were observed in the weight of the mice belonging to the various treatment groups, indicating lack of general lymphatic effects or overt toxicity (data not shown). Reduced density of tumor lymphatics was also seen in C8161 melanoma xenografts of mice treated with the LSD conjugate (data not shown).

To study the mechanism of the lymphatic disruption by the REA conjugate, we examined the frequency of apoptosis in lymphatic endothelial cells in PPC1 tumors using caspase-3 as a marker. The tumors of the mice treated with the REA conjugate had a significant increase in lymphatic endothelial cells expressing active caspase-3 compared with tumors of mice treated with PBS, REA, or a mixture of REA and $_D(KLAKLAK)_2$ (Fig. 6*C*). These data indicate that the REA conjugate reduced the lymphatic vessel counts by inducing apoptosis in lymphatic endothelial cells.

Discussion

In this article, we show an extensive heterogeneity of tumor lymphatics. We have identified peptides that recognize the lymphatics of individual tumor types, including transgenic mouse tumors arising *de novo* in different organs, as well as human tumor xenografts. We also describe a peptide that distinguishes the lymphatics of premalignant prostatic lesions, both from normal lymphatics and from those of fully developed tumors in the same transgenic mouse model of prostate carcinogenesis. The lymphatic

Table 1. Main characteristics of lymphatic homing peptides

Peptide	Tumor used to isolate homing peptide	Tumors tested for phage homing *in vivo**	Specific homing †	Fold over control phage
LSD	C8161 s.c. xenografts	C8161 xenografts	Yes	39
		KRIB xenografts	Yes	7 ‡
		K14-HPV16 skin cancer	No	5
		MDA-MB-435 orthotopic xenografts	No	3
		MMTV-PyMT breast tumors	No	3
		PPC1 orthotopic xenografts	No	3
		TRAMP prostate tumors	No	1
REA	TRAMP prostate tumors	TRAMP prostate tumors	Yes	46
		PPC1 orthotopic xenografts	Yes	25
		M12 orthotopic xenografts	Yes	24
		LNCaP orthotopic xenografts	Yes	20
		DU145 orthotopic xenografts	Yes	14
		MMTV-PyMT breast tumors	Yes	8 ‡
		K14-HPV16/E_2 cervical cancer	Yes	7 ‡
		KRIB xenografts	Yes	7 ‡
		PPC1 s.c. xenografts	No	6
		C8161 s.c. xenografts	No	5
		K14-HPV16 skin cancer	No	4
		MDA-MB-435 orthotopic xenografts	No	4
AGR	TRAMP PIN lesions	TRAMP PIN lesions	Yes	18
		TRAMP prostate tumors	No	4
		K14-HPV16/E_2 cervical dysplasia	No	5
		K14-HPV16/E_2 cervical tumors	No	4
		MMTV-PyMT premalignant lesions	No	2
		MMTV-PyMT breast tumors	No	4
LyP-2	K14-HPV16 skin cancer	K14-HPV16/E_2 cervical dysplasia	Yes	17
		K14-HPV16/E_2 cervical tumors	Yes	22
		MDA-MB-435 orthotopic xenografts	No	3

*TRAMP, MMTV-PyMT, and K14-HPV16 are genetically engineered mouse models of organ-specific carcinogenesis, each of which presents first with angiogenic dysplasia and subsequently carcinoma.

†The specific homing of phage is considered to be strong (>10-fold compared with control), weak (between 5- and 10-fold), or nonspecific (below 5-fold).

‡Phage homing corroborated by fluorescent peptide homing.

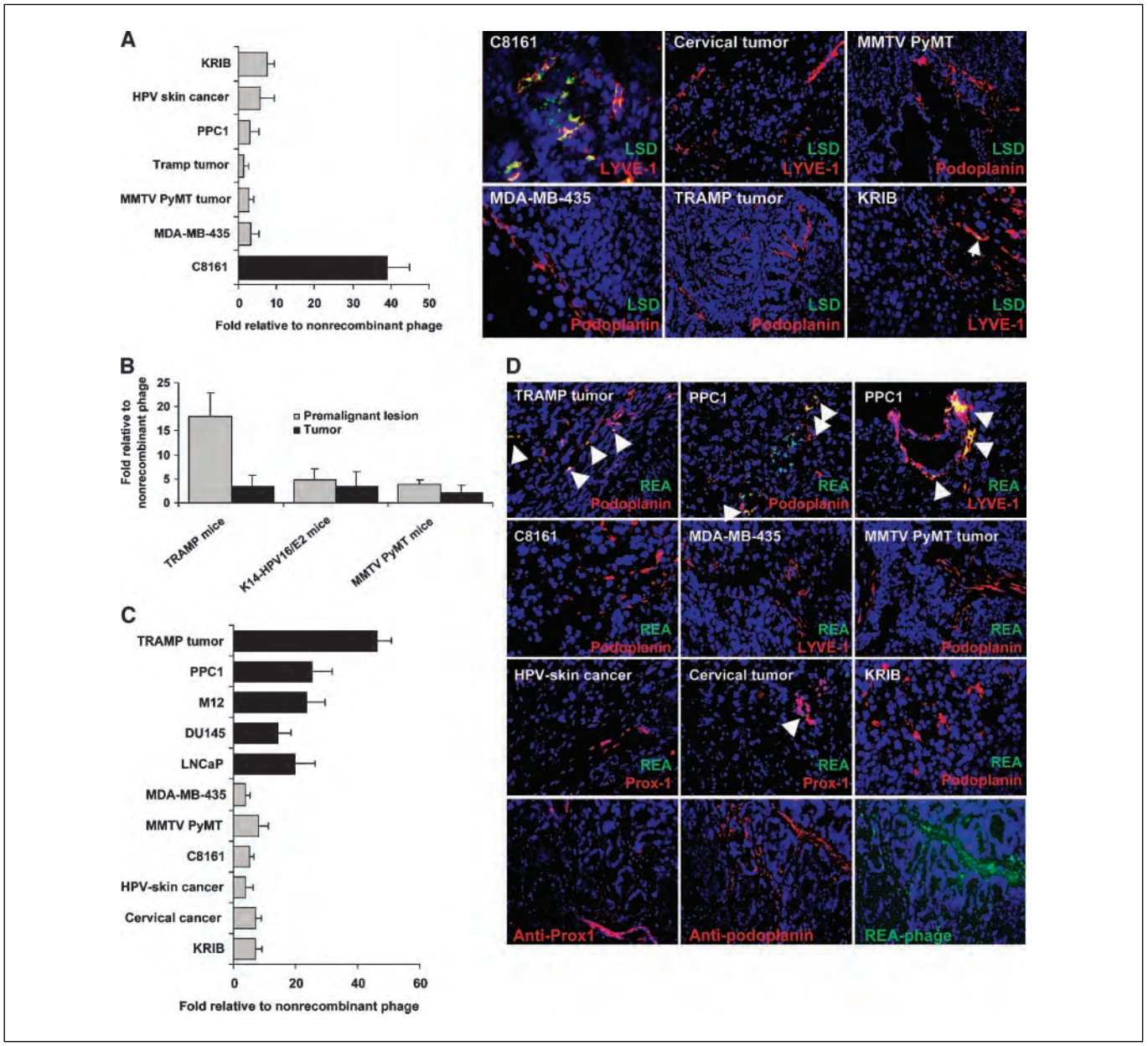

Figure 4. Homing specificity of the LSD, REA, and AGR peptides in different types of tumors and premalignant lesions. *In vivo* homing of the LSD phage (*A, left*) and fluorescein-labeled LSD peptide (*A, right*) to six types of tumors was tested as in Fig. 1 (n = 3-6). Robust phage homing and peptide fluorescence was only observed in C8161 tumors. KRIB xenograft tumors were slightly positive for phage and peptide homing, but phage homing to C8161 tumors was significantly higher than to this or any of the other tumors ($P < 0.005$). Original magnification, ×400. *B, in vivo* homing of i.v. injected AGR phage in TRAMP mice, K14-HPV16/E_2 mice bearing CIN-3 lesions or tumors (n = 3), and MMTV-PyMT mice with dysplastic lesions or breast tumors. The AGR phage homed significantly more to TRAMP premalignant lesions than to comparable lesions in the other tumor models ($P < 0.03$). *In vivo* homing of the REA phage (*C*) and fluorescein-labeled REA peptide (*D*) to 11 types of tumors was tested (n = 3-6). Significant phage homing and peptide fluorescence was observed in prostate tumors of TRAMP mice, and in PPC1, M12, DU145, and LNCaP human prostate cancer xenograft tumors (peptide fluorescence is shown for PPC1 in *D*). Four of five prostate cancers (DU145 was the exception) accumulated significantly more REA phage than the other types of tumors ($P < 0.03$). Cervical tumors in K14-HPV16/E_2 mice were slightly positive. REA phage overlay of primary human prostate cancer is shown in *D* (*bottom row*). Human tumor tissue sections were stained with Prox-1 or antipodoplanin. A serial section from the podoplanin staining was used for REA phage overlay showing correspondence of the podoplanin and the REA phage localization.

markers detected by the homing peptides are specific for lymphatic vessels (i.e., the peptides do not bind to the blood vessels of the same tumors or premalignant lesions). Several prostate cancers shared the same lymphatic marker. These results show that the lymphatics express a zip code system that is akin to the one in blood vessels, but distinct from it. In beginning, to assess the applications of this knowledge, we showed that systemic treatment of tumor-bearing mice with a lymphatic homing peptide linked to a proapoptotic compound could selectively destroy tumor lymphatics.

We used a new screening method based on the immunoisolation of lymphatic endothelial cells from whole tumor cell suspensions that had been preincubated with phage display libraries, thereby enriching for phage bound to this rare cell type. This method allowed us to focus on the selection of phage-displayed peptides that identify specific features in the lymphatics

of the target tissue. We show in each of the tumor models that peptides strongly represented in the selected phage pools specifically homed to tumors, and extensively colocalized with markers of lymphatic endothelial cells in the tumor tissue after an i.v. injection. In contrast, there was no colocalization with blood vessel endothelial markers. Costaining with the lymphatic markers LYVE-1, podoplanin, Prox-1, and VEGFR3 were consistent in supporting this result. The use of multiple markers is an important standard, as none of the lymphatic endothelial markers is completely specific for lymphatics (30, 31). In aggregate, however, they provide strong evidence for a lymphatic vessel identity of the structures that our peptide recognizes in tumors.

We have now shown lymphatic vessel specialization in every one of the five tumor types studied. These tumors consisted of xenograft models of melanoma, breast, and prostate carcinomas, as well as transgenic mouse models developing prostate, skin, and cervical cancers. In addition, the LSD, REA, and LyP peptides each recognized tumor lymphatics in more than one inbred mouse strain. For example, the REA peptide homed to prostate cancers in TRAMP mice (C57BL/6 background) and prostate cancer xenograft tumors grown in nude mice (BALB/c), demonstrating that their specificity is not limited to any given mouse strain. Previous studies have defined a peptide that distinguishes the lymphatics of MDA-MB-435 breast cancer xenografts tumors from normal lymphatics (13, 25). The present results show that such molecular specialization of tumor lymphatics is not limited to this tumor, but is likely to be a generalized phenomenon. The peptides we identified in this study as being specific for lymphatic vessels in the various tumor models were essentially specific for the tumor type used in the screening. Interestingly, the only other tumors with lymphatics recognized by the TRAMP tumor-homing peptide REA were xenograft tumors generated with four different human prostate cancer cell lines. This result suggests that the changes detected by our peptides in tumor lymphatics may be tumor type specific. Similar experiments with tumor blood vessels have revealed two classes of peptides identifying signatures of the angiogenic neovasculature. One pan-specific class recognizes markers that are generally associated with angiogenesis in most tumor types and organs (1, 4, 32, 33), whereas a second class of peptides detected tumor type–specific vascular signatures (7, 8). Although we did not isolate any peptides that identified pan-specific markers of tumor (but not normal) lymphatics, we anticipate that additional screens could reveal such entities.

Stage-specific lymphatic signatures during tumorigenesis. We obtained two stage-specific lymphatic homing peptides using different neoplastic lesions in the TRAMP model. The REA peptide selectively recognizes the lymphatics in fully developed TRAMP tumors, whereas the AGR peptide was only reactive with the lymphatics in PIN lesions. Our laboratories have previously obtained homing peptides that distinguish the blood vessels of premalignant lesions from normal blood vessels and those of malignant tumors arising subsequently in the same transgenic mouse models (7, 8). The present results suggest that lymphatic vessels display a similar evolution of molecular specificities as tumorigenesis progresses.

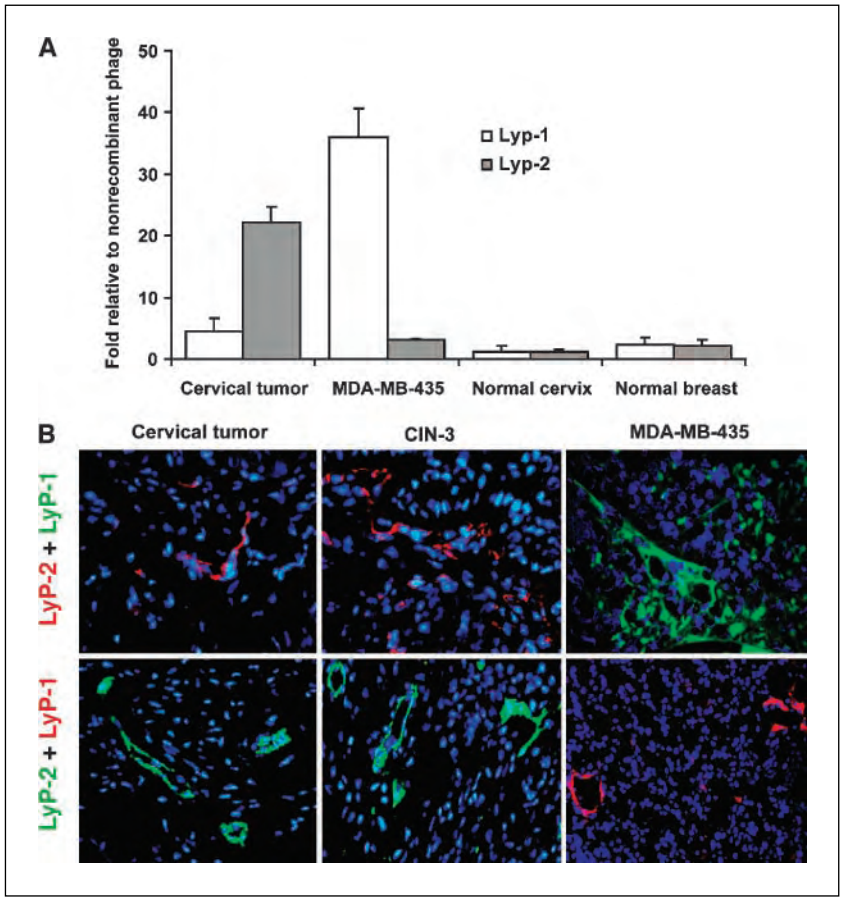

Figure 5. Differential tumor-homing specificity of LyP-1 and LyP-2 peptides. *A,* LyP-1 and LyP-2 phage were i.v. injected into mice bearing MDA-MB-435 breast cancer xenografts or K14-HPV16/E_2 tumors (n = 3). *B,* fluorescein-labeled LyP-1 and rhodamine-labeled LyP-2 (*top row*) were i.v. injected (100 μg of each peptide) into the mice bearing tumors or premalignant lesions. Alternatively, the injection consisted of rhodamine-labeled LyP-1 and fluorescein-labeled LyP-2 (*bottom row*). Tissues were collected and processed for histologic analysis 2 hours later. LyP-1 homes to the MDA-MB-435 tumors, whereas LyP-2 homes to the cervical cancers and premalignant lesions. Phage homing to the premalignant lesions was significantly higher than to the corresponding tumors in both models ($P < 0.01$). Original magnification, ×400.

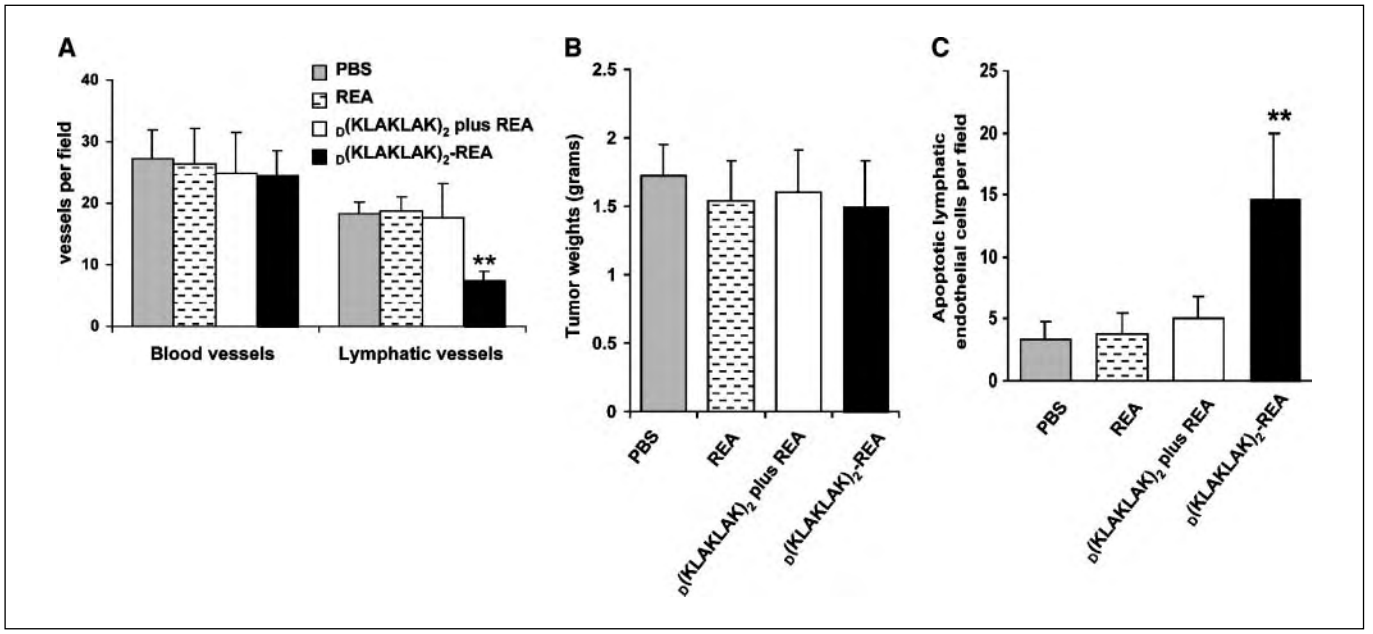

Figure 6. Targeting the tumor-associated lymphatics with homing peptides linked to a proapoptotic peptide. The PPC1 orthotopic xenografted mice (10 mice per group) were systemically treated with 100 μg/dose/mouse/biweekly of $_D$(KLAKLAK)$_2$-CREAGRKAC, equimolar amounts of the uncoupled peptides, or with the vehicle (PBS). At termination, tumor weights were recorded and frozen tissue sections were prepared for immunohistochemical analysis. *A,* the $_D$(KLAKLAK)$_2$-CREAGRKAC chimeric peptide greatly reduces the number of tumor lymphatics ($P < 0.01$) as determined from podoplanin staining, whereas the blood vessel count (MECA-32 staining) and tumor volume (*B*) were unaffected. *C,* $_D$(KLAKLAK)$_2$-CREAGRKAC induced apoptosis of lymphatic endothelial cells in PPC1 tumors. The apoptotic lymphatic endothelial cells were detected by double staining with antiactive caspase-3 and antipodoplanin antibodies. A significant increase in apoptosis of lymphatic endothelial cells in PPC1 tumors was observed in tumors of mice treated with the $_D$(KLAKLAK)$_2$-CREAGRKAC conjugate compared with controls ($P < 0.001$).

A prospective family of lymphatic signatures? The mutually exclusive tumor specificity of the LyP-1 and LyP-2 peptides is interesting given the close sequence similarity of these peptides (CGNKRTRGC versus CNRRTKAGC). LyP-1 recognizes lymphatics and tumor cells in MDA-MB-435 and MMTV-PyMT breast cancers (8). Careful comparison of the ability of the two peptides to accumulate in MDA-MB-435 tumors and cervical carcinomas after i.v. injection showed that MDA-MB-435 tumors were positive for LyP-1, whereas cervical carcinomas were not, whereas LyP-2 had the opposite specificity. Interestingly, both peptides bound to other cell types in the neoplastic lesions: LyP-1 binds to and is internalized by breast tumor cells, whereas LyP-2 binds to scattered cells in the neoplastic cervix. The bases for and the implications of these distinctive lymphatic and non-lymphatic binding specificities are presently unclear and deserve future investigation. We have encountered a third peptide in the LyP series, CNKRTRGGC. We did not include that peptide in this study but its specificity seems to parallel that of LyP-1 (25). Comparison of the three sequences indicates that shifting the glycine residue from the NH_2-terminal to the COOH-terminal end is not important to the specificity of the peptide, but that the arrangement of the basic residues in the K/RRTR/K motif can alter specificity. Our attempts to identify the binding molecules (receptors) for the LyP peptides (and indeed for other of the lymphatic signature–finding peptides identified in this study) have not been successful thus far, and this remains an agenda for future studies. The closely related sequences of the LyP peptides predict the existence of a family of related receptors with tumor type–specific expression in lymphatics. The distinctive specificity of peptides containing the RGD motif in different sequence contexts for individual integrins (34) exemplifies the archetype.

Prospects for therapeutic and diagnostic targeting of the lymphatics. The peptides we describe here have potentially important uses. Early targeting of the tumor lymphatics for destruction may serve to reduce metastatic spread, as lymphatic vessels provide one of the main routes for the spreading of many types of cancer (15–17, 35, 36). In the present study, we were able to reduce the abundance of lymphatics in melanoma xenograft tumors by using lymphatic homing peptides to direct a toxic peptide to the lymphatics in these tumors. In agreement with earlier studies (36), the destruction of the lymphatics had little effect on the growth of the melanoma tumors. These data support the proposition that primary tumor growth is not in general dependent on the lymphatic neovasculature. However, targeted destruction of tumor lymphatics with homing peptide conjugates has prospect to limit metastatic dissemination as has been exemplified in other studies that genetically manipulated lymphatic growth factors to eliminate tumor lymphatics (15–17, 35, 36).

Although studying the effect of the lymphatic homing peptide-drug conjugates on metastasis is one of our long-term aims, we foresee considerable potential in more general applications aimed at producing antitumor effects with homing peptides for tumor lymphatics. Lymphatic homing peptides can be harnessed to deliver a payload into the tumor, as illustrated herein for fluorescein and for the $_D$(KLAKLAK)$_2$ proapototic peptide. Targeted drug conjugates can potentially have broader effects than what can be obtained by destroying peritumoral lymphatics. Homing peptides for tumor blood vessels have been used in targeted delivery of therapeutic agents into tumors. As a result of such targeting, the efficacy of the drug increased, whereas its side effects were reduced (26, 32, 37, 38). Our lymphatic homing peptides present another potential route for targeted delivery of drugs into tumors.

Tumor-specific changes in the lymphatics may also have applications in diagnostic molecular imaging of tumor growth, progression, and response to therapy, as well as for early detection of incipient organ-specific cancers (or premalignant progenitor lesions) that evidently have both blood and lymphatic vascular signatures.

Acknowledgments

Received 11/7/2005; revised 2/8/2006; accepted 4/4/2006.

Grant support: NIH grants PO1 CA 82713 (E. Ruoslahti and D. Hanahan), PO1 CA 104898, and RO1 CA115410 (E. Ruoslahti); Cancer Center support grant P30 CA 30199 (The Burnham Institute) and other grants from the National Cancer Institute/NIH (D. Hanahan); Department of Defense grant DAMD 17-02-1-0315 (E. Ruoslahti); fellowship DAMD17-02-0309 from the Department of Defense (L. Zhang); and National Cancer Institute training grant T32 CA77109-05 (J.A. Hoffman).

The costs of publication of this article were defrayed in part by the payment of page charges. This article must therefore be hereby marked *advertisement* in accordance with 18 U.S.C. Section 1734 solely to indicate this fact.

We thank Dr. Rania Kairouz for her participation in the early stages of this work; Dr. Fernando Ferrer for peptide syntheses; Dr. Daniel Mercola for human prostate cancer samples; Robbin Newlin, Cherry Concengco, and Katie Gilliland for technical assistance with histology; and Roslind Varghese for editing.

References

1. Ruoslahti E. Specialization of tumour vasculature. Nat Rev Cancer 2002;2:83–90.
2. Hanahan D, Weinberg RA. The hallmarks of cancer. Cell 2000;100:57–70.
3. Brooks PG, Clouse J, Morris LS. Hysterectomy vs. resectoscopic endometrial ablation for the control of abnormal uterine bleeding. A cost-comparative study. J Reprod Med 1994;39:755–60.
4. Christian S, Pilch J, Akerman ME, Porkka K, Laakkonen P, Ruoslahti E. Nucleolin expressed at the cell surface is a marker of endothelial cells in angiogenic blood vessels. J Cell Biol 2003;163:871–8.
5. Ferrara N, Alitalo K. Clinical applications of angiogenic growth factors and their inhibitors. Nat Med 1999;5: 1359–64.
6. Pasqualini R, Koivunen E, Kain R, et al. Aminopeptidase N is a receptor for tumor-homing peptides and a target for inhibiting angiogenesis. Cancer Res 2000;60: 722–7.
7. Hoffman JA, Giraudo E, Singh M, et al. Progressive vascular changes in a transgenic mouse model of squamous cell carcinoma. Cancer Cell 2003;4:383–91.
8. Joyce JA, Laakkonen P, Bernasconi M, Bergers G, Ruoslahti E, Hanahan D. Stage-specific vascular markers revealed by phage display in a mouse model of pancreatic islet tumorigenesis. Cancer Cell 2003;4: 393–403.
9. Cao R, Bjorndahl MA, Religa P, et al. PDGF-BB induces intratumoral lymphangiogenesis and promotes lymphatic metastasis. Cancer Cell 2004;6:333–45.
10. Cassella M, Skobe M. Lymphatic vessel activation in cancer. Ann N Y Acad Sci 2002;979:120–30.
11. Stacker SA, Achen MG, Jussila L, Baldwin ME, Alitalo K. Lymphangiogenesis and cancer metastasis. Nat Rev Cancer 2002;2:573–83.
12. Jackson DG, Prevo R, Clasper S, Banerji S. LYVE-1, the lymphatic system and tumor lymphangiogenesis. Trends Immunol 2001;22:317–21.
13. Laakkonen P, Porkka K, Hoffman JA, Ruoslahti E. A tumor-homing peptide with a targeting specificity related to lymphatic vessels. Nat Med 2002;8:751–5.
14. Padera TP, Kadambi A, di Tomaso E, et al. Lymphatic metastasis in the absence of functional intratumor lymphatics. Science 2002;296:1883–6.
15. Mandriota SJ, Jussila L, Jeltsch M, et al. Vascular endothelial growth factor-C-mediated lymphangiogenesis promotes tumour metastasis. EMBO J 2001;20: 672–82.
16. Skobe M, Hawighorst T, Jackson DG, et al. Induction of tumor lymphangiogenesis by VEGF-C promotes breast cancer metastasis. Nat Med 2001;7:192–8.
17. Saharinen P, Tammela T, Karkkainen MJ, Alitalo K. Lymphatic vasculature: development, molecular regulation and role in tumor metastasis and inflammation. Trends Immunol 2004;25:387–95.
18. Bae VL, Jackson-Cook CK, Maygarden SJ, Plymate SR, Chen J, Ware JL. Metastatic sublines of an SV40 large T antigen immortalized human prostate epithelial cell line. Prostate 1998;34:275–82.
19. Arbeit JM, Munger K, Howley PM, Hanahan D. Progressive squamous epithelial neoplasia in K14-human papillomavirus type 16 transgenic mice. J Virol 1994;68:4358–68.
20. Arbeit JM, Howley PM, Hanahan D. Chronic estrogen-induced cervical and vaginal squamous carcinogenesis in human papillomavirus type 16 transgenic mice. Proc Natl Acad Sci U S A 1996;93:2930–5.
21. Giraudo E, Inoue M, Hanahan D. An aminobisphosphonate targets MMP-9-expressing macrophages and angiogenesis to impair cervical carcinogenesis. J Clin Invest 2004;114:623–33.
22. Hoffman J, Laakkonen P, Porkka K, Bernasconi M, Ruoslahti E. *In vivo* and *ex vivo* selections using phage-displayed libraries. In: Clackson T, Lowman HB, editors. Phage display. New York: Oxford University Press; 2004. p. 171–92.
23. Greenberg NM, DeMayo F, Finegold MJ, et al. Prostate cancer in a transgenic mouse. Proc Natl Acad Sci U S A 1995;92:3439–43.
24. Gingrich JR, Greenberg NM. A transgenic mouse prostate cancer model. Toxicol Pathol 1996;24:502–4.
25. Laakkonen P, Akerman ME, Biliran H, et al. Antitumor activity of a homing peptide that targets tumor lymphatics and tumor cells. Proc Natl Acad Sci U S A 2004;101:9381–6.
26. Ellerby HM, Arap W, Ellerby LM, et al. Anti-cancer activity of targeted pro-apoptotic peptides. Nat Med 1999;5:1032–8.
27. Arap W, Haedicke W, Bernasconi M, et al. Targeting the prostate for destruction through a vascular address. Proc Natl Acad Sci U S A 2002;99:1527–31.
28. Hsu CX, Ross BD, Chrisp CE, et al. Longitudinal cohort analysis of lethal prostate cancer progression in transgenic mice. J Urol 1998;160:1500–5.
29. Coussens LM, Hanahan D, Arbeit JM. Genetic predisposition and parameters of malignant progression in K14-16 transgenic mice. Am J Pathol 1996;149:1899–917.
30. Mouta Carreira C, Nasser SM, di Tomaso E, et al. LYVE-1 is not restricted to the lymph vessels: expression in normal liver blood sinusoids and down-regulation in human liver cancer and cirrhosis. Cancer Res 2001;61: 8079–84.
31. Valtola R, Salven P, Heikkila P, et al. VEGFR-3 and its ligand VEGF-C are associated with angiogenesis in breast cancer. Am J Pathol 1999;154:1381–90.
32. Arap W, Pasqualini R, Ruoslahti E. Chemotherapy targeted to tumor vasculature. Curr Opin Oncol 1998;10: 560–5.
33. Yao VJ, Ozawa MG, Trepel M, Arap W, McDonald DM, Pasqualini R. Targeting pancreatic islets with phage display assisted by laser pressure catapult microdissection. Am J Pathol 2005;166:625–36.
34. Ruoslahti E. The RGD story: a personal account. Matrix Biol 2003;22:459–65.
35. Stacker SA, Caesar C, Baldwin ME, et al. VEGF-D promotes the metastatic spread of tumor cells via the lymphatics. Nat Med 2001;7:186–91.
36. Lin J, Lalani AS, Harding TC, et al. Inhibition of lymphogenous metastasis using adeno-associated virus-mediated gene transfer of a soluble VEGFR-3 decoy receptor. Cancer Res 2005;65:6901–9.
37. Curnis F, Gasparri A, Sacchi A, Longhi R, Corti A. Coupling tumor necrosis factor-α with αV integrin ligands improves its antineoplastic activity. Cancer Res 2004;64:565–71.
38. Curnis F, Sacchi A, Borgna L, Magni F, Gasparri A, Corti A. Enhancement of tumor necrosis factor α antitumor immunotherapeutic properties by targeted delivery to aminopeptidase N (CD13). Nat Biotechnol 2000;18:1185–90.

Antiangiogenic Therapy Decreases Integrin Expression in Normalized Tumor Blood Vessels

Virginia J. Yao,[1] Michael G. Ozawa,[1] Amanda S. Varner,[1] Ian M. Kasman,[1] Yvan H. Chanthery,[1] Renata Pasqualini,[3] Wadih Arap,[3] and Donald M. McDonald[1,2]

[1]Department of Anatomy, [2]Cardiovascular Research Institute, Comprehensive Cancer Center, University of California, San Francisco, California; and [3]The University of Texas M.D. Anderson Cancer Center, Houston, Texas

Abstract

Tumor blood vessels normalized by antiangiogenic therapy may provide improved delivery of chemotherapeutic agents during a window of time but it is unknown how protein expression in tumor vascular endothelial cells changes. We evaluated the distribution of RGD-4C phage, which binds $\alpha_v\beta_3$, $\alpha_v\beta_5$, and $\alpha_5\beta_1$ integrins on tumor blood vessels before and after antiangiogenic therapy. Unlike the control phage, fd-tet, RGD-4C phage homed to vascular endothelial cells in spontaneous tumors in RIP-Tag2 transgenic mice in a dose-dependent fashion. The distribution of phage was similar to $\alpha_v\beta_3$ and $\alpha_5\beta_1$ integrin expression. Blood vessels that survived treatment with AG-013736, a small molecule inhibitor of vascular endothelial growth factor and platelet-derived growth factor receptors, had only 4% as much binding of RGD-4C phage compared with vessels in untreated tumors. Cellular distribution of RGD-4C phage in surviving tumor vessels matched the $\alpha_5\beta_1$ integrin expression. The reduction in integrin expression on tumor vessels after antiangiogenic therapy raises the possibility that integrin-targeted delivery of diagnostics or therapeutics may be compromised. Efficacious delivery of drugs may benefit from identification by *in vivo* phage display of targeting peptides that bind to tumor blood vessels normalized by antiangiogenic agents. (Cancer Res 2006; 66(5): 2639-49)

Introduction

The morphologic, organizational, and metabolic diversity of endothelial cells exemplifies the heterogeneity of the microvasculature (1). In the brain, continuous endothelial cells of the blood-brain barrier restrict the movement of solutes, whereas fenestrated endothelial cells of the choroid plexus favor solute flux (2). Signals from endothelial cells influence the formation of bone (3) and the development of the pancreas and liver from the primitive endoderm (4, 5). Compared with quiescent established blood vessels, endothelial cells in angiogenic blood vessels express additional proteins, such as the $\alpha_v\beta_3$, $\alpha_v\beta_5$ (6–8) and the $\alpha_5\beta_1$ integrins (9). Peptides that bind specifically to distinct vascular beds in normal mice and in a human subject, as identified by *in vivo* phage display, show the inherent molecular heterogeneity within the microvasculature (1, 10, 11). Intraorgan vascular heterogeneity has also been shown by two peptide phage that are ephrin A-type ligand mimetics that bind solely to the vasculature of normal murine pancreatic islets with increased localization to islet tumor blood vessels (12). Given such inherent molecular diversity of the normal and tumor microvasculature, resident receptor proteins for selective targeting of diagnostic and therapeutic agents to specific vascular beds can be identified and exploited.

An example of a tumor-targeting phage is one displaying the sequence, CDCRGDCFC (termed RGD-4C phage). The double cyclic RGD-4C peptide binds with a 200-fold greater *in vitro* affinity to $\alpha_v\beta_3$ and $\alpha_v\beta_5$ integrins and a 50-fold greater affinity to the $\alpha_5\beta_1$ integrin than the linear GRGDSP peptide (13). Moreover, *in vivo* studies show RGD-4C phage have a 40- to 80-fold greater selectivity for tumor blood vessels (8). Tumor burden decreased upon i.v. delivery of the RGD-4C peptide fused to either doxorubicin or to a proapoptotic peptide with reduced host toxicity (14, 15). Other studies revealed FITC-labeled RGD-4C peptide binds to both human MDA-MB-435 tumor xenografts and infiltrating murine tumor endothelial cells (16).

In addition to site-directed targeting, inhibition of proangiogenic factors and their signaling pathways has shown promise as tumor therapies (17, 18). Tumor blood vessel regression is enhanced when therapeutic regimens combine vascular endothelial growth factor receptor (VEGFR)-2 inhibitors, such as SU5416, with platelet-derived growth factor receptor (PDGFR)-β inhibitors, such as SU6668 or Gleevec (19), in implanted rat gliomas and pancreatic islet tumors (20, 21). We have recently shown that VEGF Trap, a soluble VEGFR-1/VEGFR-2 chimeric antibody that binds VEGF-A, VEGF-B, and placental growth factor-1 (22), and AG-013736, a potent small molecule inhibitor of VEGF/PDGF receptor tyrosine kinases (23), cause the disappearance of endothelial fenestrations, tumor vessel regression, and the appearance of basement membrane ghosts in murine pancreatic islet tumors (24). Although combination therapies using antiangiogenic compounds with chemotherapy are successful (25, 26), the timing for administration of secondary therapeutic(s) via the normalized tumor vasculature is likely to be a critical factor (27, 28). Although the surviving normalized tumor vessels are functional, molecular changes to the tumor endothelium following antiangiogenic therapy are less well understood.

In this study, we examined the physiologic distribution of the tumor-targeting RGD-4C phage by immunofluorescence microscopy in blood vessels of the RIP-Tag2 pancreatic islet tumor mouse model (29) and its distribution following AG-013736 therapy. The first objective of this study was to compare the distribution of RGD-4C versus fd-tet phage in tumor blood vessels. We sought to quantify the dose dependency of phage distribution and to corroborate the distribution of $\alpha_v\beta_3$ and $\alpha_5\beta_1$ integrins to that of RGD-4C phage in tumor blood vessels. In addition, we compared the targeted localization of RGD-4C phage in tumor blood vessels to normal blood vessels in the lung, thyroid gland, cerebral cortex, and liver. Our second objective was to determine whether RGD-4C

Requests for reprints: Donald M. McDonald, University of California, San Francisco, 513 Parnassus Avenue, S1363, San Francisco, CA 94143-0452. Phone: 415-476-6616; Fax: 415-476-4845; E-mail: dmcd@itsa.ucsf.edu.

doi:10.1158/0008-5472.CAN-05-1824

phage could be used as a biological tool to determine whether endothelial cells that survive antiangiogenic therapy modify their pattern of integrin expression, thereby signaling a phenotypic change in the vasculature.

Materials and Methods

Animals. RIP-Tag2 transgenic mice from a C57BL/6 background contain the insulin promoter–driven SV40 T-antigen and produce spontaneous multifocal and multistage pancreatic islet tumors (29). RIP-Tag2-positive mice were genotyped from tail-tip DNA by PCR. Male and female RIP-Tag2 mice and nontransgenic littermates between 8 and 12 weeks of age were used in these studies. Mice were housed under barrier conditions at the animal care facility at the University of California, San Francisco. The Institutional Animal Care and Use Committee at University of California, San Francisco, approved all experimental procedures.

Phage preparation. Purified single-stranded fd-tet (30) or CDCRGDCFC (13) phage DNA was electroporated into competent MC1061 *Escherichia coli* (31), and plated onto Luria-Bertani agar medium containing 100 mg/L streptomycin and 40 mg/L tetracycline (LB/Strep/TET). Single colonies were picked, peptide inserts were amplified by colony PCR, and sequences were verified (12). Phages were amplified overnight at 37°C with agitation from a single transformed MC1061 colony in 100 mL LB/Strep/TET. Phage were precipitated from the bacterial supernatant with 15% NaCl/PEG 8000 (Fisher Scientific, Tustin, CA) for 1 hour on ice, pelleted by centrifugation for 20 minutes at 4°C at 10,400 × *g*, gently resuspended in 5 mL sterile PBS, and precipitated with 15% NaCl/PEG 8000 on ice for 30 minutes. The final phage pellet was gently resuspended in 100 μL sterile PBS, centrifuged for 2 minutes at maximum *g* force, and the supernatant was filtered through a 0.22 μm syringe filter. Infectivity titers were determined using established protocols (32).

Phage and antibody injections and tissue preparation. Purified, titered phage preparations were used within 24 hours of preparation. Serial dilutions of phage at 10^9, 10^8, and 10^7 transforming units (TU) were made with DMEM containing Earle salts (University of California, San Francisco Cell Culture Facility) to a final volume of 200 μL. Twenty-five micrograms hamster CD61 (PharMingen, San Diego, CA), rat CD51 (eBioscience, San Diego, CA), monoclonal rat CD49e antibodies (PharMingen), or corresponding amounts of normal hamster (Jackson ImmunoResearch, West Grove, PA) or rat serum antibodies (Jackson ImmunoResearch) were diluted with sterile saline to a final volume of 125 μL each and filtered through 0.22 μm filters. Phage and antibodies were administered i.v. into Avertin (2,2,2-tribromoethanol, 0.015-0.017 mg/g, injected i.p., Sigma-Aldrich Corp., St. Louis, MO)–anesthetized mice (32) and allowed to circulate for 6 minutes. Body temperatures of anesthetized mice were maintained with a heating pad. Mice were systemically perfused with 1% paraformaldehyde in PBS, pH 7.4, and tissues were frozen (12).

AG-013736 treatment. Nine-week-old male RIP-Tag2 mice (n = 10) were injected with either AG-013736 (25 mg/kg, i.p., BID) or with the vehicle [three parts PEG 400 to seven parts acidified H_2O (pH 2)] for 7 days. AG-013736 is a potent small molecule inhibitor of VEGF/PDGF receptor tyrosine kinases (IC_{50}, 1.2 nmol/L for VEGFR-1, 0.25 nmol/L for VEGFR-2, 0.29 nmol/L for VEGFR-3, 2.5 nmol/L for PDGFR-β, 2.0 nmol/L for c-Kit, and 218 nmol/L for FGFR-1; ref. 23), and was provided by Pfizer Global Research and Development (San Diego, CA). Treated mice were injected i.v. with 10^9 TU RGD-4C phage and perfused as described above.

Immunohistochemistry. Details for immunostaining fixed frozen sections and sections of phage injected tissues were previously described (12). For immunostaining antibody-injected tissues, sections were incubated with either monoclonal Armenian hamster anti-mouse CD31 (1:1,000, Chemicon, Temecula, CA) or monoclonal rat antimouse CD31 antibodies (1:500, PharMingen) and 5% normal goat serum (Jackson ImmunoResearch) with 1% Triton X-100 in PBS (PBST; pH 7.4). Rinsed sections were incubated in secondary antibody solutions containing goat FITC-conjugated anti-rat antibodies (1:200, Jackson ImmunoResearch) and goat Cy3-conjugated anti-Armenian hamster antibodies (1:400, Jackson ImmunoResearch), or goat FITC-conjugated anti-Armenian hamster antibodies (1:200, Jackson Immuno Research), or goat Cy3-conjugated anti-rat antibodies (1:400, Jackson ImmunoResearch) and 5% normal goat serum in PBST. Triple stained sections were incubated with monoclonal rat anti-mouse CD31, monoclonal Cy3-conjugated α-smooth muscle actin (α-SMA, 1:2,000, Sigma-Aldrich), rabbit polyclonal anti-fd-bacteriophage antibody (1:5,000, Sigma-Aldrich), and 5% normal mouse serum in PBST. Rinsed sections were incubated in a secondary antibody solution containing mouse FITC-conjugated anti-rat IgGs, mouse Cy5-conjugated anti-rabbit IgGs (1:400, Jackson ImmunoResearch), and 5% normal mouse serum in PBST. For the AG-013736 studies, frozen 80 μm sections from vehicle or AG-013736-treated tissues were incubated with monoclonal Armenian hamster anti-mouse CD31 and monoclonal rat CD49e antibodies (1:500, PharMingen) and 5% normal goat serum in PBST. Rinsed sections were incubated in a secondary antibody solution containing goat FITC-conjugated anti-Armenian hamster antibodies and goat Cy3-conjugated anti-rat antibodies in PBST.

Imaging. Fluorescence images were acquired using an externally coded, three-chip charge-coupled device camera (CoolCam, SciMeasure Analytical Systems, Atlanta, GA) fitted on a Zeiss Axiophot fluorescence microscope with Fluar objectives or with a Zeiss LSM 510 Laser Scanning confocal microscope with krypton-argon and helium-neon lasers at 488, 543, and 633 nm (Carl Zeiss, Jena, Germany) and analyzed with the Zeiss LSM 510 software v. 3.2.2.

Quantification of phage in blood vessels. Densities of phage immunoreactivity in blood vessels, hereafter called phage vessel area density, for the dose-dependent studies were quantified from 20-μm-thick confocal projections of immunostained RIP-Tag2 islets using ImageJ (http://rsb.info.nih.gov/ij/) with the Zeiss LSM Reader plug-in interface (http://rsb.info.nih.gov/ij/plugins/lsm-reader.html). Total blood vessel densities of tumor islets were determined from CD31-immunoreactive blood vessels and calculated from user-defined islet regions after thresholds were empirically determined. Phage vessel area densities were calculated as the number of pixels of phage immunoreactivity divided by the total vessel area represented by CD31 immunoreactivity. Mean phage vessel area density values and SEs were determined from five islet tumors or acinar regions each from three mice injected with 10^9, 10^8, and 10^7 TU RGD-4C phage, and five islet tumors each from three mice injected with 10^9, 10^8, and 10^7 TU fd-tet phage. For the buffer control, five to six islet tumors each were analyzed from five mice. For the AG-013736 studies, phage vessel area densities were quantified from digital Coolcam fluorescence images acquired with a ×10 Fluar objective. Phage vessel area densities were determined as the percentage of red pixels (phage) to the total number of green pixels (CD31) in islets using the threshold setting of 50 for each image. Mean ± SE values were calculated from five images per mouse (n = 5 mice per group). Statistical analyses were determined by the ANOVA Bonferroni-Dunn test. Cy3 anti-rat CD49e fluorescence intensities of 80 μm pancreatic immunostained sections from vehicle and AG-013736-treated mice were measured from digitized Coolcam images acquired with a ×20 Fluar objective. Cy3 digitized images were converted to grayscale 8-bit images using the look-up table importer plug-in in ImageJ. A customized look-up table that defines the boundaries of fluorescence intensities as a spectrum of color from 0 to 255 was applied to each 8-bit image that was then converted to a surface plot. Increased fluorescence intensities correspond to increased peak heights in the Z-plane.

Results

Distribution of RGD-4C phage in tumor blood vessels. Tumors in RIP-Tag2 transgenic mice were used as a model because they are multifocal and multistage, thereby allowing visualization of phage in tumor blood vessels during various stages of tumorigenesis as well as in normal blood vessels in the acinar pancreas. The immunohistochemical staining pattern of i.v. administered 10^9 TU of RGD-4C phage in the tumor vasculature was distinct and punctate (Fig. 1). In RIP-Tag2 tumors, RGD-4C phage was abundant in blood vessels 6 minutes after injection such that the majority of the tumor

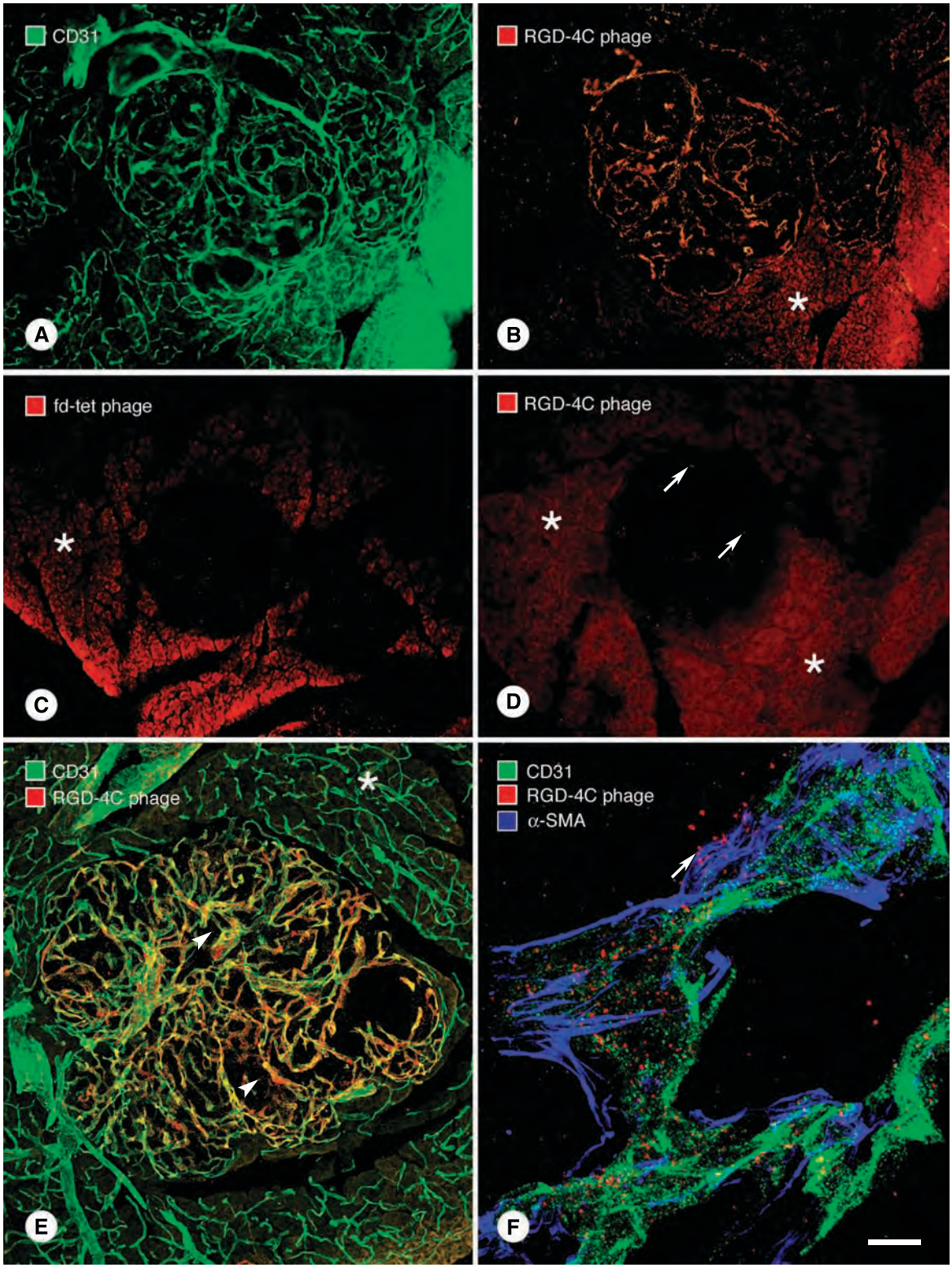

Figure 1. Localization of 10^9 TU RGD-4C phage to RIP-Tag2 islet tumor blood vessels. *A,* blood vessels (CD31, *green*) in two RIP-Tag2 tumors contain (*B*) RGD-4C phage (*red*). RIP-Tag2 tumor blood vessels contain negligible amounts of (*C*) fd-tet phage (*red*), whereas (*D*) vessels in normal islets contain a minimal amount of RGD-4C phage (*red, arrows*). RGD-4C or fd-tet phage show minimal binding to blood vessels in the acinar pancreas from either RIP-Tag2 or C57BL/6 mice (*B-D, asterisks*). *E,* RGD-4C phage (*red*) colocalize with blood vessels (*green*) in a RIP-Tag2 tumor with small focal regions of extravasated phage (*arrowheads*), whereas acinar blood vessels do not contain RGD-4C phage (*asterisk*). *F,* at high magnification, RGD-4C phage (*red*) are primarily confined within tumor blood vessels (*green*); however, extravasated phage (*arrow*) outside blood vessels do not colocalize with associated pericytes (α-SMA, *blue*). Bar in (*F*) applies to all panels: *A* to *C,* 160 μm; *D,* 80 μm; *E,* 60 μm; *F,* 13 μm.

vasculature could be delineated by RGD-4C phage immunoreactivity (Fig. 1*A* and *B*). In contrast, an equivalent amount of the insertless, negative control phage, fd-tet, did not localize to tumor blood vessels (Fig. 1*C*); RGD-4C phage localized much less to blood vessels in normal islets (Fig. 1*D, arrows*). RGD-4C phage accumulation was not influenced by tumor size and was distributed throughout the tumor vasculature with focal regions of extravasation (Fig. 1*E, arrowheads*). Moreover, the amount of RGD-4C phage was comparatively low to none in the acinar pancreas blood vessels of either RIP-Tag2 or normal mice (Fig. 1*B-E, asterisks*). Extravasated RGD-4C phage did not seem to colocalize with α-SMA-immunoreactive pericytes (Fig. 1*F, arrow*).

Quantification of RGD-4C phage in tumor blood vessels. The affinity of RGD-4C phage binding to blood vessels in RIP-Tag2 tumors was examined further by decreasing the injected dose from 10^9 to 10^7 TU (Fig. 2). We reasoned that if *in vivo* binding of RGD-4C phage was a specific event, then our immunofluorescence studies should show a reduction of phage binding commensurate with decreasing amounts of i.v. administered phage. These experiments should also provide information regarding the threshold for phage detection by immunohistochemistry. The amount of RGD-4C phage in blood vessels in RIP-Tag2 tumors was reduced when the amount of injected phage decreased from 10^9 to 10^7 TU (Fig. 2*A-C*). Background immunostaining in tumor blood vessels from buffer-treated control mice was negligible (data not shown). RGD-4C phage was detectable when injected at 10^7 TU (Fig. 2*C, right*); however, the immunoreactivity was comparable with fd-tet phage injected at 10^7 TU (data not shown). Mean RGD-4C and fd-tet phage vessel area densities were quantified in CD31-immunoreactive tumor blood vessels at each dose (Fig. 2*D*). At 10^9 TU, the mean RGD-4C phage vessel area density was 4-fold greater than that of fd-tet phage in tumor blood vessels and was statistically significant

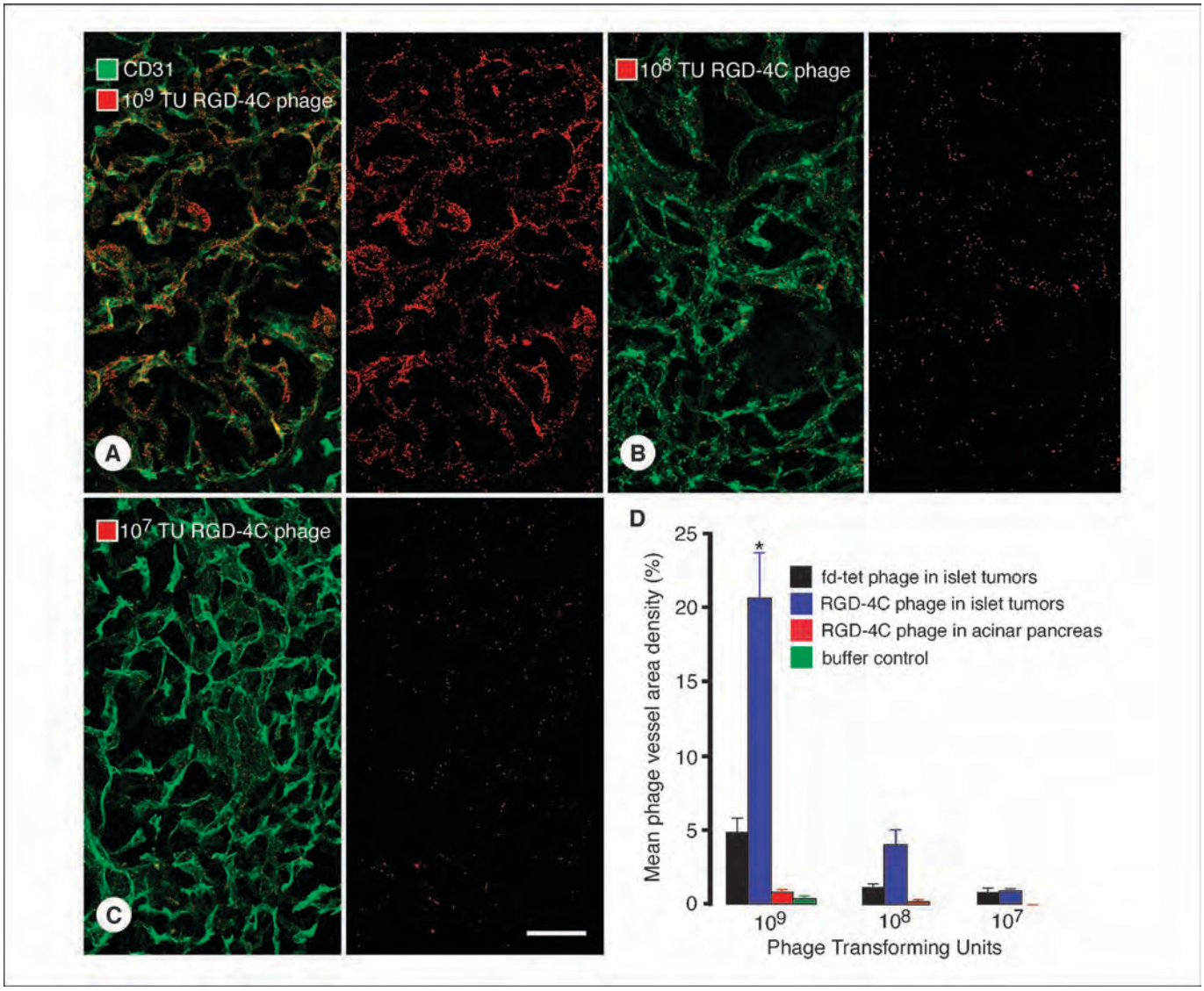

Figure 2. Dose-dependent RGD-4C phage distribution in RIP-Tag2 tumor blood vessels. *A* to *C,* identical confocal images are split: *left,* phage immunoreactivity (*red*) in blood vessels (CD31, *green*); *right,* phage immunoreactivity only. RGD-4C phage distribution in RIP-Tag2 tumor blood vessels from mice receiving (*A*) 10^9, (*B*) 10^8, and (*C*) 10^7 TU RGD-4C phage decreases with decreasing dose. *D,* quantification of mean phage vessel area densities show the amount of RGD-4C phage in the tumor islet vasculature at 10^9 TU was ~4-fold greater than fd-tet phage, whereas mean RGD-4C and fd-tet phage area densities were similar at 10^7 TU. Bonferroni-Dunn analysis of the mean RGD-4C phage area density in islet tumor blood vessels compared with acinar vessels at the 10^9 TU dose was statistically significant (*$P < 0.0027$). Bar in (*C*) applies to all panels (*A-C*), 26 μm.

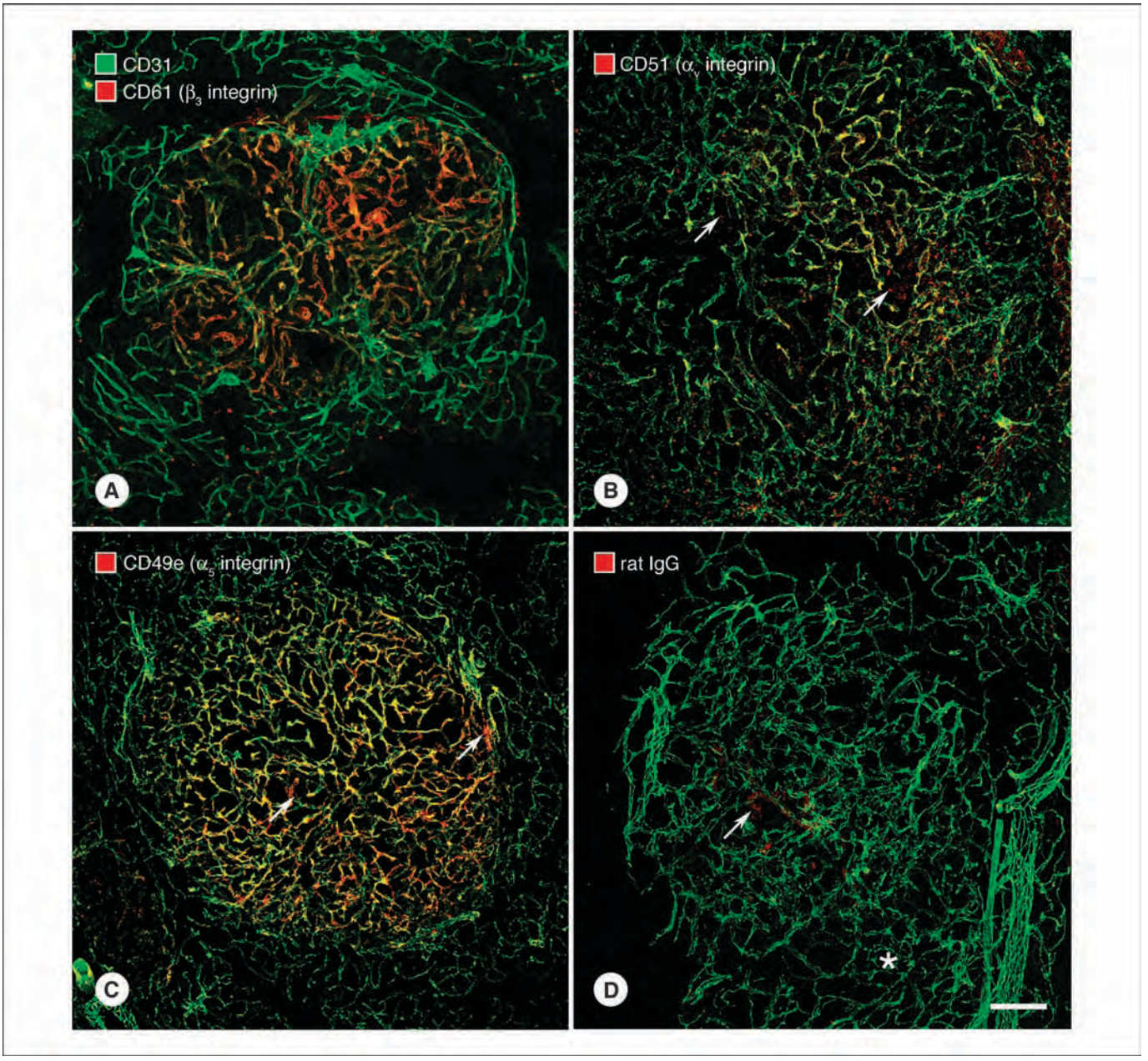

Figure 3. Luminal β_3, α_v, and α_5 integrin expression in RIP-Tag2 tumor vessels. Confocal images of RIP-Tag2 pancreatic islet tumors show heterogeneous expression of (*A*) β_3 integrin (CD61, *red*), and (*B*) α_v integrin (CD51, *red*) in tumor blood vessels (CD31, *green*). Immunoreactivity of α_v integrin is weaker than that of the β_3 integrin in tumor blood vessels. *C,* α_5 integrin expression (CD49e, *red*) is homogenous throughout the islet tumor vasculature (*green*). *D,* immunoreactivity of injected control normal rat serum antibodies (*red*) in tumor blood vessels (*green*) was minimal and similar to their localization in the acinar blood vessels (*asterisk*). Leakage of α_v (*B, arrows*), α_5 integrin antibodies (*C, arrows*), and rat IgGs (*D, arrow*) is apparent outside the tumor vasculature. Bar in (*D*) applies to all panels: *A* and *D,* 53 μm; *B,* 132 μm; and *C,* 64 μm.

compared with the amount of RGD-4C phage found in normal blood vessels of the acinar pancreas. The amount of RGD-4C phage found in the acinar pancreas blood vessels at this dose was similar to the background immunoreactivity measured in islet tumors from buffer-injected RIP-Tag2 control mice. At 10^8 TU, the mean RGD-4C phage area density in tumor blood vessels was 3.4-fold greater than that of fd-tet phage. Mean phage vessel area densities for RGD-4C and fd-tet phages were similar at the injected dose of 10^7 TU. Unlike RGD-4C phage, the mean fd-tet phage vessel area density in tumor blood vessels was similar when injected into RIP-Tag2 mice at either 10^8 or 10^7 TU.

Molecular specificity of RGD-4C phage localization in tumor blood vessels. Given that the RGD peptide is the recognition sequence for many adhesive proteins, such as the $\alpha_v\beta_3$, $\alpha_v\beta_5$, and $\alpha_5\beta_1$ integrins (33), we sought to evaluate the molecular specificity of RGD-4C phage localization by examining the *in vivo* distribution of the α_v, β_3, and α_5 integrins in RIP-Tag2 tumor blood vessels (Fig. 3). Similar to the phage immunostaining pattern, β_3 integrin (CD61, a binding partner of α_v integrin), immunoreactivity in blood vessels of RIP-Tag2 tumors was not uniformly distributed (Fig. 3*A*). Some blood vessels were strongly stained whereas others were devoid of β_3 integrin immunoreactivity.

α_v Integrin (CD51) immunoreactivity was weaker and nonuniformly distributed in tumor blood vessels as well (Fig. 3*B*). Consistent with recent reports (34, 35), α_5 integrin (CD49e) immunoreactivity and, hence, $\alpha_5\beta_1$ integrin expression, because this integrin is a unique heterodimer (33), was strong and uniformly distributed throughout the tumor blood vessels and was not detectable in adjacent normal acinar blood vessels (Fig. 3*C*). Neither control hamster (data not shown) nor rat serum antibodies colocalized with tumor blood vessels or normal blood vessels in the acinar pancreas (Fig. 3*D, asterisk*). Extravasation of α_v, α_5, and rat serum antibodies from tumor blood vessels was apparent outside tumor blood vessels (Fig. 3*B-D, arrows*).

Distribution of RGD-4C phage in other tissues. In contrast to its distribution in tumor blood vessels, negligible amounts of RGD-4C phage were found in blood vessels of the lung (Fig. 4*A*) and in capillaries surrounding the thyroid follicles (Fig. 4*B*), whereas phages were not detected in the cerebral cortex (Fig. 4*C*). Interestingly, by increasing the input of RGD-4C phage to 5×10^9 TU, we observed phage in blood vessels of the cerebral cortex (data not shown). Phage immunoreactivity was distinct, punctate, and evenly distributed within the hepatic endothelial sinusoids such that the sinusoids (Fig. 4*D, arrow*) surrounding each central vein (Fig. 4*D, arrowhead*) were delineated by phage immunoreactivity. Rapid clearance of phage by the reticuloendothelial system and corresponding accumulation of phage in the liver as determined by bacterial infection (8) are consistent with our observations of identical high amounts of RGD-4C phage (Fig. 4*D*) or fd-tet phage immunoreactivity in the murine liver and spleen (data not shown) after a 6-minute circulation time. The half-life of injected fd-tet phage in the blood was ~5.5 minutes and recovery of fd-tet phage from the C57BL/6 mouse liver 6 minutes postinjection was typically 4% of total injected phage in a nonsaturated system (data not shown). After a 60-minute circulation, fd-tet phage was not detected in hepatocytes but were present in Kupffer cells with the majority of fd-tet phage associated with sinusoidal endothelial cells (data not shown).

Reduced RGD-4C phage localization after AG-013736 treatment. Preferential localization of RGD-4C phage to the tumor vasculature prompted us to examine whether the distribution of RGD-4C phage in tumor blood vessels following treatment of

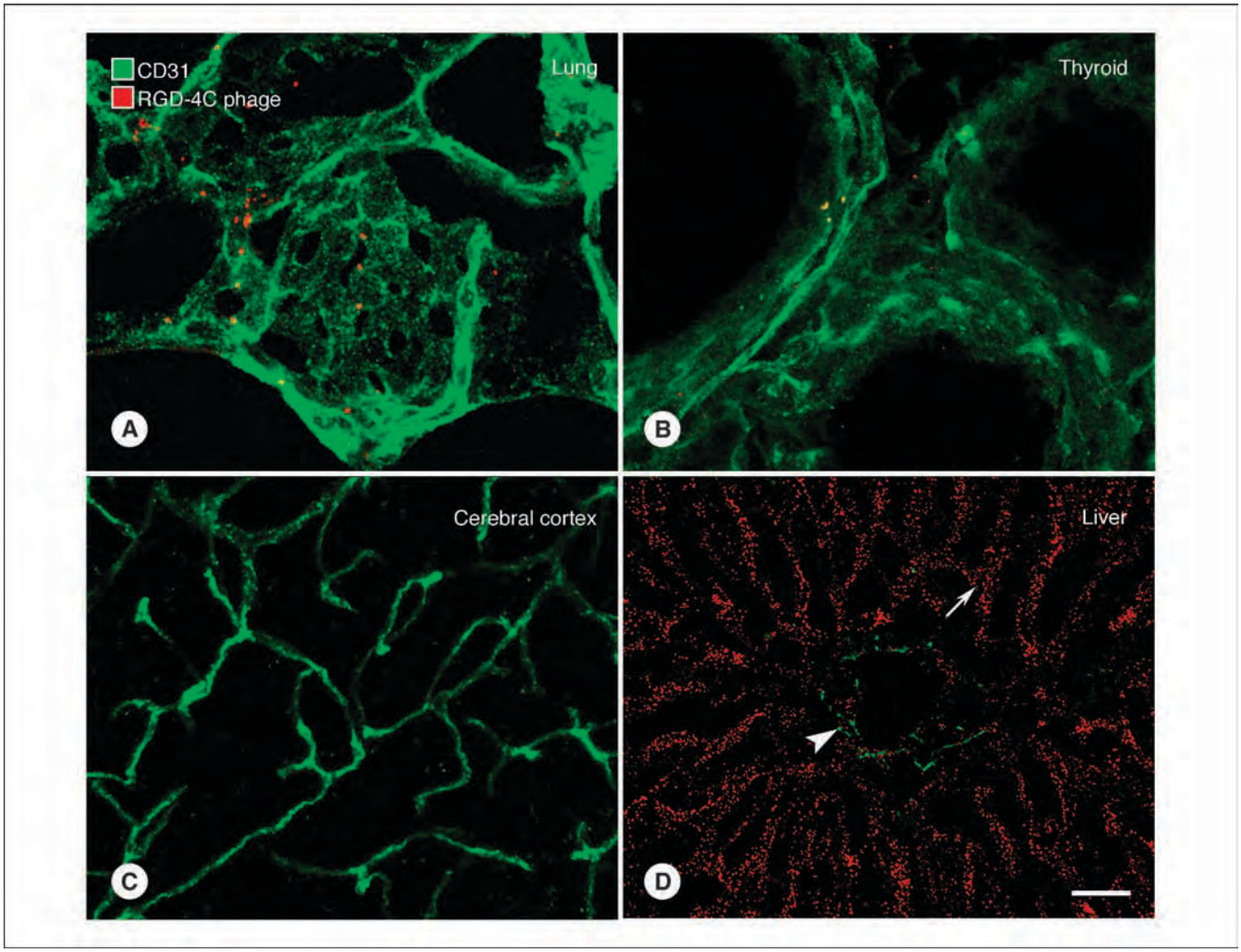

Figure 4. Distribution of RGD-4C and fd-tet phage in normal blood vessels. RGD-4C phage immunoreactivity (*red*) in blood vessels (CD31, *green*) of the RIP-Tag2 (*A*) lung, (*B*) thyroid gland, and (*C*) cerebral cortex is low to none in these normal blood vessels after a 6-minute circulation. *D,* distribution of RGD-4C phage immunoreactivity (*red*) in the liver is largely constrained within the sinusoidal endothelium (*arrow*) that drain toward a central vein whose borders are CD31 immunoreactive (*green, arrowhead*). Bar in (*D*) applies to all panels: *A,* 7 μm; *B* and *D,* 13 μm; *C,* 27 μm.

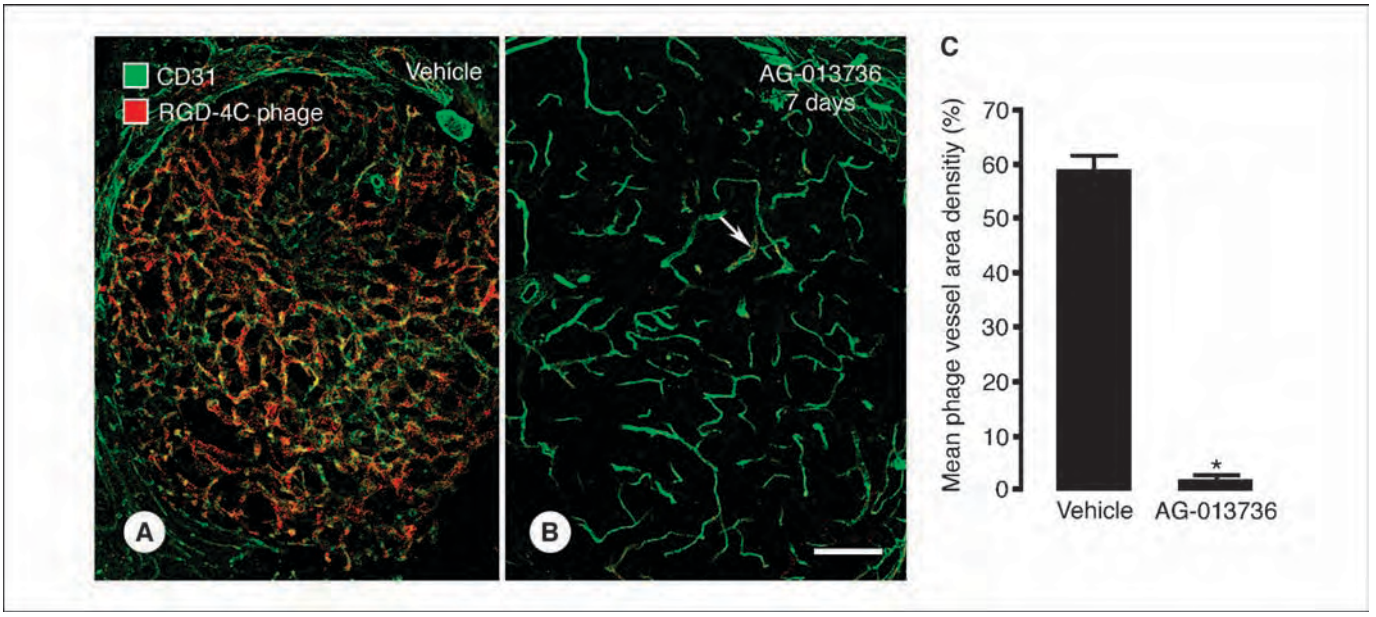

Figure 5. RGD-4C phage localization decreases in blood vessels after AG-013736 treatment. *A,* RGD-4C phage (*red*) colocalize with CD31-immunoreactive tumor blood vessels (*green*) from RIP-Tag2 mice treated with vehicle for 7 days. *B,* surviving blood vessels following AG-013736 treatment for 7 days contain variable and lower amounts of RGD-4C phage (*red, arrow*). *C,* the mean phage vessel area density quantified from islet blood vessels of vehicle versus AG-013736-treated mice show that RGD-4C phage binding is reduced to 4% in the AG-013736-normalized tumor vasculature. Bonferroni-Dunn analysis of the mean phage vessel area density between vehicle-treated and AG-013736-treated islet vasculature was statistically significant (*, $P < 0.0001$). Bar in (*B*) applies to (*A* and *B*): *A,* 106 μm; *B,* 132 μm.

RIP-Tag2 mice with AG-013736 would be altered (Fig. 5). We reasoned that if tumor blood vessels are normalized (28) following AG-013736 treatment, the amount of RGD-4C phage bound *in vivo* would reflect a difference in endothelial cell integrin expression. Pancreatic sections from vehicle-treated mice injected with RGD-4C phage 6 minutes before perfusion showed strong phage immunoreactivity in tumor blood vessels (Fig. 5*A*) that was similar to islet vessels in untreated RIP-Tag2 mice (compare with Fig. 1*B* and *E*). Conversely, RGD-4C phage localization in islet blood vessels was greatly reduced in AG-013736-treated mice (Fig. 5*B, arrow*). Blood vessels in the AG-013736-treated tumors had notably uniform diameters and decreased tortuosity than vehicle-treated tumors as previously reported (24). RGD-4C phage area density in the AG-013736-treated islet vasculature was ~4% of that quantified from vehicle-treated vessels (Fig. 5*C*).

Reduced $\alpha_5\beta_1$ integrin expression in AG-013736-treated tumor blood vessels. To understand the molecular basis for the marked decrease of RGD-4C phage distribution in the surviving islet blood vessels of AG-013736-treated mice, the expression of the $\alpha_5\beta_1$ integrin was evaluated in vehicle versus AG-013736-treated pancreatic sections by immunohistochemistry (Fig. 6). Expression of $\alpha_5\beta_1$ was chosen because its expression was robust and uniform in untreated RIP-Tag2 tumor blood vessels (Fig. 3*C*). In vehicle-treated mice, $\alpha_5\beta_1$ integrin expression in tumor blood vessels was similar to that found in untreated RIP-Tag2 mice (Fig. 6*A* and *B*). Alternatively, $\alpha_5\beta_1$ integrin immunoreactivity in the remaining islet blood vessels from mice treated with AG-013736 for 7 days was much less and heterogeneous (Fig. 6*C* and *D*). In some islet blood vessels, $\alpha_5\beta_1$ integrin expression was strong (Fig. 6*C* and *D, arrow*), whereas expression was weak (Fig. 6*C* and *D, yellow arrowhead*) or absent in other blood vessels (Fig. 6*C* and *D, white arrowhead*). Acinar blood vessels were also $\alpha_5\beta_1$ immunoreactive because the antibody was not administered i.v.. $\alpha_5\beta_1$ Integrin fluorescence intensity in vehicle versus AG-013736-treated islet blood vessels of large islet tumors was decreased in the latter (Fig. 6*E* and *F*). Qualitative differences of $\alpha_5\beta_1$ integrin fluorescence intensities in the corresponding surface plot illustrate significantly decreased peak heights in surviving islet blood vessels from AG-013736-treated mice (Fig. 6*G*).

Discussion

We show the *in vivo* cellular distribution of RGD-4C phage by immunofluorescence microscopy is highly sensitive and reflects the expression of vascular receptors. We established RGD-4C phage colocalize with CD31-immunoreactive tumor blood vessels and that extravasation of phage from tumor blood vessels occurs in focal regions within a few minutes. Quantification of phage area density in tumor blood vessels showed a dose dependency that is consistent with specific binding and to α_v, α_5, and β_3 integrin expression. Treatment of RIP-Tag2 mice with AG-013736 markedly decreased the amount of RGD-4C phage bound to surviving blood vessels, which was consistent with decreased $\alpha_5\beta_1$ integrin expression. RGD-4C phage binding to the normal endothelium was barely detectable, whereas systemic clearance of phage occurred mainly via the hepatic sinusoidal endothelial cells.

Differential integrin expression in vehicle versus AG-013736-treated blood vessels. Consistent with earlier reports (6–9), our studies show the $\alpha_v\beta_3$ and $\alpha_5\beta_1$ integrins that bind the RGD-4C phage in normal blood vessels were up-regulated in tumor blood vessels. Following AG-013736 treatment, our studies showed endothelial expression of the $\alpha_5\beta_1$ integrin was substantially down-regulated. Studies using primary endothelial cells isolated from human umbilical cord veins show $\alpha_v\beta_3$, $\alpha_5\beta_1$, and $\alpha_2\beta_1$ integrins are physically associated with $VEGF_{165}$-bound VEGFR-2 (36, 37). Moreover, endothelial cell migration and proliferation are

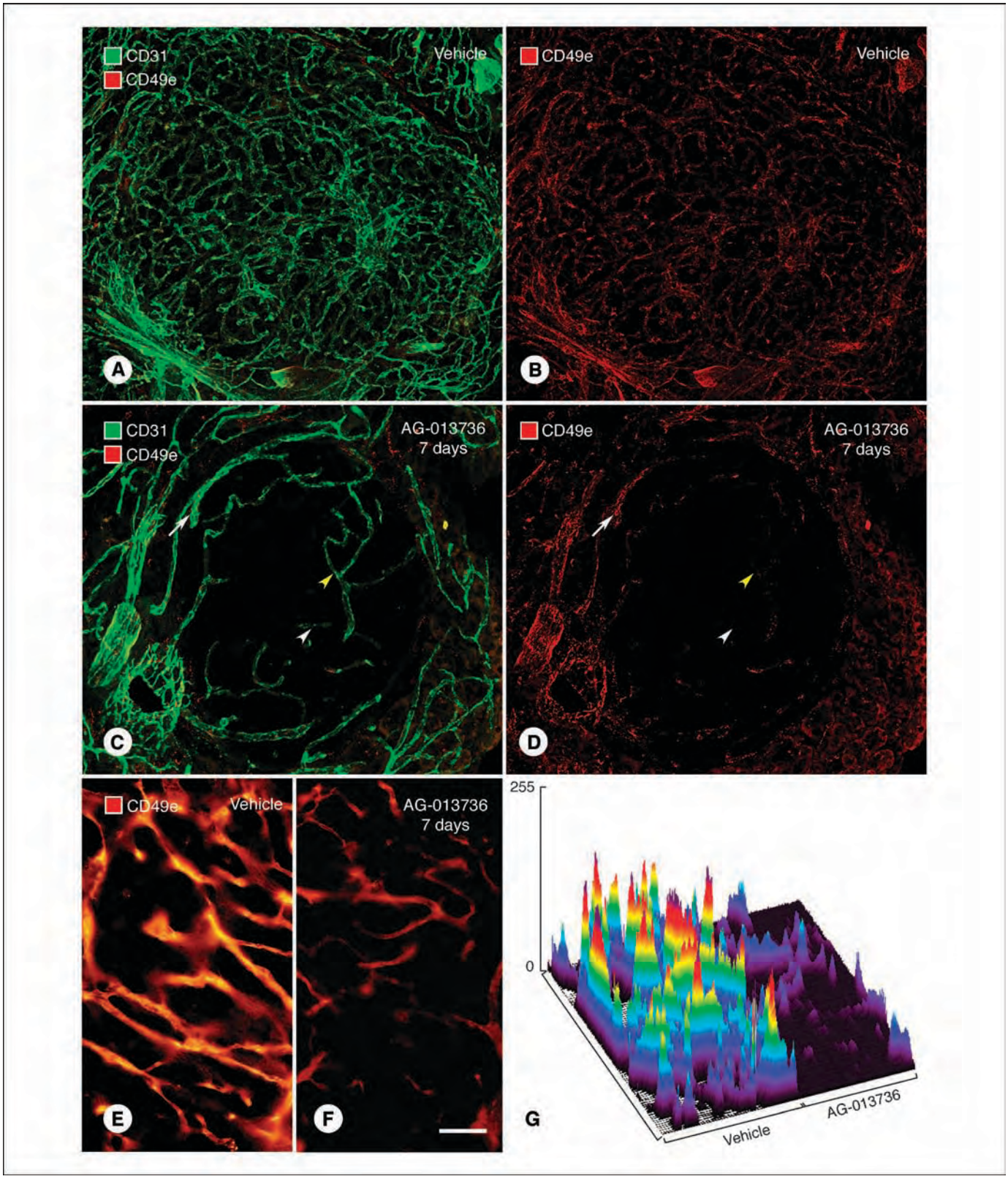

Figure 6. $\alpha_5\beta_1$ Integrin expression decreases in AG-013736-treated islet blood vessels. *A* and *B,* tumor blood vessels (CD31, *green*) in pancreatic islets from vehicle and AG-013736-treated RIP-Tag2 mice show robust homogeneous $\alpha_5\beta_1$ integrin immunoreactivity (CD49e, *red*) of blood vessels immunostained on pancreatic tissue sections from vehicle-treated mice, whereas (*C* and *D*) surviving islet blood vessels in AG-013736-treated mice show strong (*arrow*), weak (*yellow arrowhead*), or no (*white arrowhead*) $\alpha_5\beta_1$ integrin expression. Qualitative comparison of $\alpha_5\beta_1$ immunofluorescence intensities of blood vessels from large islet tumors between (*E*) vehicle and (*F*) AG-013736-treated mice shows (*G*) markedly decreased vascular $\alpha_5\beta_1$ integrin expression in AG-013736-treated RIP-Tag2 mice. Bar in (*F*) applies to (*A-F*): *A* and *B,* 106 μm; *C* and *D*, 53 μm; *E* and *F,* 60 μm.

enhanced when cells were plated on vitronectin, fibronectin, and type I collagen, the primary cognate ligands for $\alpha_v\beta_3$, $\alpha_5\beta_1$, and $\alpha_2\beta_1$ integrins, respectively. Adhesion proteins, such as fibronectin, vitronectin, laminin, as well as collagen, contain the RGD binding motif as recognized by the $\alpha_v\beta_3$, $\alpha_5\beta_1$, and $\alpha_2\beta_1$ integrins, respectively (33). The presence of basement membrane ghosts lacking endothelial cells in AG-013736-treated RIP-Tag2 islet tumors (24) is consistent with our current finding of integrin down-regulation because integrins mediate cell adhesion to the basement membrane. Others have shown decreased endothelial cell expression of integrins such as $\alpha_2\beta_1$ may account for the loss of capillary lumen maintenance and tube formation (38). We have shown decreased expression of VEGFR-2 and VEGFR-3 in AG-013736-treated RIP-Tag2 tumors (24). Thus, down-regulation of VEGF receptors by AG-013736 and decreased RGD-4C binding to AG-013736-treated tumors may have effectively disrupted the crosstalk between VEGF and adhesion receptors (39, 40). Whether integrin expression is down-regulated as a result of inhibiting VEGFR-2 signaling cascades or by directly inhibiting integrin transcription is unknown. The net effect of AG-013736 treatment in RIP-Tag2 tumors indicates that the surviving tumor blood vessels are functional and have decreased levels of integrin expression despite the high VEGF concentration in these tumors (41). Our results suggest that AG-013736 therapy may act synergistically with integrin antagonists (42) in combination therapy to effect a faster rate of tumor blood vessel regression.

Pericyte changes associated with AG-013736 treatment. Comparison of pericyte morphology in wild-type mice to the RIP-Tag2 tumor mouse model (43) and a mouse model of prostate cancer (44) show pericytes are loosely associated with tumor blood vessels, have processes that extend away from the vessel wall, overlap with other pericytes, and accompany and extend beyond endothelial sprouts. Due to the heterogeneity of islet tumors in the RIP-Tag2 model, the amount of α-SMA-immunoreactive pericytes increases with tumor size, whereas vessels in hyperplastic islets have mostly desmin-immunoreactive pericytes (43). Subsequent to this work, Inai et al. (24) showed pericyte processes are more tightly associated with normalized blood vessels in tumors from RIP-Tag2 mice treated with AG-013736 for 7 days by scanning electron microscopy. An interesting finding of this work is that although the area density of CD31-immunoreactive blood vessels decreases by 79% following AG-013736 treatment, the reduction of α-SMA-immunoreactive pericyte area density (33%) is not coincident with vessel regression but is similar to the reduction of basement membrane area density. Indeed, immunohistochemistry with all three marker proteins, α-SMA, CD31, and type IV collagen, shows the α-SMA-immunoreactive pericytes associate with either normalized blood vessels or with basement membrane sleeves that do not contain endothelial cells. Recent studies showed that pericytes of RIP-Tag2 mice treated with AG-013736 for 7 days and then withdrawn from treatment for 4 days reverted to that morphology described by Morikawa et al (43).[4] Immunohistochemical studies using antibodies that recognize PDGFR-β showed the area density of PDGFR-β-immunoreactive pericytes was unchanged in the absence or presence of AG-013736 and after AG-013736 treatment was withdrawn. Consistent with earlier studies (24), however, the ratio of α-SMA and PDGFR-β area densities decreased during AG-013736 treatment and returned to baseline levels 7 days after withdrawal of AG-013736. These results suggest sustained AG-013736 treatment reverted pericyte protein expression to a normal phenotype rather than decreased the total number of pericytes. The biochemical transformation of pericytes following AG-013736 treatment corresponds with their gross morphologic changes to a more normal phenotype (24). Whether vessel normalization and pericyte transformation occurs concurrently or in a sequential fashion is unknown. Decreased endothelial expression of $\alpha_5\beta_1$ integrin and the findings of pericyte transformations upon treatment with a broad-spectrum compound, such as AG-013736, lends further support for effective treatment of tumors with combination therapies.

Physiologic evaluation of tumor blood vessels by RGD-4C phage. Recent reports show that combination therapies of antiangiogenic inhibitors are more efficacious when used with low-dose chemotherapy (25–27). In addition, because tumors activate multiple angiogenic pathways, others propose that clinical therapies should include cocktails of angiogenic inhibitors that target multiple angiogenic pathways (18, 28). The paradox of abrogating tumor blood vessels in antiangiogenic therapy when delivery of therapeutics is dependent on a functional vasculature can be resolved because angiogenic inhibitors gradually "prune" the dysfunctional tumor vasculature to a more "normalized" state (28). The period in which the normalized functional vasculature can be effectively used to deliver appropriate therapeutics, however, is a critical temporal window (26). Accurate assessment of the tumor vasculature during antiangiogenic therapy by peptide phage such as RGD-4C may provide one variable by which the rate and extent of tumor blood vessel normalization can be evaluated for appropriate application of secondary treatment regimens.

Targeting specificity of RGD-4C phage. The distribution of 10^9 TU RGD-4C in islet tumor blood vessels reflected the expression patterns of $\alpha_v\beta_3$, $\alpha_2\beta_1$, and $\alpha_5\beta_1$ immunoreactivity. Our results do not contradict the fact that many different integrins recognize the RGD binding motif (33). Nevertheless, it would be difficult to unequivocally assign RGD-4C binding to be exclusively limited to either α_v integrins or $\alpha_5\beta_1$ integrins based on the current findings described here until reliable mouse $\alpha_v\beta_3$ and $\alpha_v\beta_5$ antibodies become available. Although α_v integrins are also expressed on pericytes and tumor cells, the limited amount of RGD-4C phage extravasation we observed here may be insufficient to detect on these perivascular cell types and/or may be confined within the vascular basement membrane to allow binding to surrounding tumor cells.

We found, however, that decreasing the dose of RGD-4C phage by 10-fold did not alter its specificity for tumor blood vessels. These findings support the targeting specificity of RGD-4C phage to angiogenic tumor blood vessels and corroborates previous reports of decreased toxicity to normal tissues of RGD-4C-based delivery of targeted therapeutics (14, 15). Although targeting peptide sequences outside the context of phage confers an improved specificity, phage display is an appealing tool by which small peptides can be rapidly propagated by bacterial amplification and screened *in vivo* due to its low toxicity to mammalian cells. Given our experimental variables, we show by immunofluorescence microscopy that 10^9 TU is an optimal dose for visualization of targeting phage and may be the optimal dose for identifying peptides from a random phage library in *in vivo* phage display.

Localization of RGD-4C phage in other tissues. Although RGD-4C phage bind to tumor blood vessels, we were interested in

[4] M.R. Mancuso, et al. Rapid vascular regrowth in tumors after reversal of VEGF inhibition, submitted for publication.

exploring this further by examining normal blood vessels of other tissues from RIP-Tag2 mice that represent a variety of endothelial cell types. Given the extensive vascularity of the lung, the small amount of phage detected indicates that RGD-4C phage binding to tumor blood vessels was not determined by the concentration of endothelial cells. To address whether binding of RGD-4C phage was specific to fenestrated endothelial cells, which are abundant in RIP-Tag2 tumors and in the thyroid gland, we found a minimal amount of RGD-4C phage in the follicular capillaries of the thyroid. These results indicate that endothelial cell type was also not a key determinant in RGD-4C phage binding in the RIP-Tag2 tumor blood vessels. The brain and liver are typically treated as negative and positive control organs, respectively, in *in vivo* phage display experiments, and our results confirmed this. Identical amounts of fd-tet or RGD-4C phage in the liver suggests phage localization in the hepatic endothelial sinusoids seems to be a property of the phage protein coat and not determined by the peptide targeting sequence thereby confirming previous findings (8).

Although *in vitro* phage display was originally developed to map antigenic sites on antibodies *in vitro* (45), this method was successfully adapted to identify *in vivo* vascular addresses in mice and in a human subject (1, 12, 46–49). Our studies here show that visualization of targeting phage in blood vessels at the cellular level by immunofluorescence microscopy allows direct identification and quantification of phage homing to the endothelium of tumor blood vessels. Decreased vascular localization of RGD-4C phage following AG-013736 treatment is consistent with down-regulation of integrin expression during normalization of surviving tumor blood vessels. Decreased integrin expression on tumor vascular endothelial cells raises the possibility of impaired targeting of chemotoxins that are dependent on integrin overexpression. These findings also illustrate the use of phage-displayed peptides as tools to probe the vascular addresses of abnormal blood vessels in disease and identify changes in the microvasculature in response to antiangiogenic treatment. Phage-displayed peptides that exploit the molecular changes in the normalized tumor endothelium may be judiciously used for targeted delivery of secondary chemotherapeutics.

Acknowledgments

Received 5/25/2005; revised 10/21/2005; accepted 12/22/2005.

Grant support: NIH grants HL-24136 and HL-59157 from the National Heart, Lung, and Blood Institute (D.M. McDonald); the Vascular Mapping Project (D.M. McDonald); National Cancer Institute grant P50-CA90270 (D.M. McDonald and W. Arap); NIH grants CA88106 (R. Pasqualini) and CA90810 (W. Arap); The Gillson-Longenbaugh Foundation and the V Foundation (R. Pasqualini and WA); and the AngelWorks Foundation (D.M. McDonald, R. Pasqualini, and W. Arap).

The costs of publication of this article were defrayed in part by the payment of page charges. This article must therefore be hereby marked *advertisement* in accordance with 18 U.S.C. Section 1734 solely to indicate this fact.

We thank Erin Ator, Michael Mancuso, and Barbara Sennino (University of California, San Francisco) for overseeing the care of the RIP-Tag2 colony; Gyulnar Baimekanova and Jie Wei (University of California, San Francisco) for genotyping the mice; Dana Hu-Lowe and David Shalinsky for providing AG-013736 (Pfizer Global Research and Development, San Diego, CA); and Jonas Fuxe and Beverly Falcón (University of California, San Francisco) for critical reading of the manuscript.

References

1. Pasqualini R, Arap W, McDonald DM. Probing the structural and molecular diversity of tumor vasculature. Trends Mol Med 2002;8:563–71.
2. Risau W. Differentiation of endothelium. FASEB J 1995;9:926–33.
3. Gerber HP, Ferrara N. Angiogenesis and bone growth. Trends Cardiovasc Med 2000;10:223–8.
4. Lammert E, Cleaver O, Melton D. Induction of pancreatic differentiation by signals from blood vessels. Science 2001;294:564–7.
5. Matsumoto K, Yoshitomi H, Rossant J, Zaret KS. Liver organogenesis promoted by endothelial cells prior to vascular function. Science 2001;294:559–63.
6. Ruoslahti E. Specialization of tumour vasculature. Nat Rev Cancer 2002;2:83–90.
7. Eliceiri BP, Cheresh DA. Role of α_v integrins during angiogenesis. Cancer J 2000;6 Suppl 3:S245–9.
8. Pasqualini R, Koivunen E, Ruoslahti E. α_v Integrins as receptors for tumor targeting by circulating ligands. Nat Biotechnol 1997;15:542–6.
9. Kim S, Bell K, Mousa SA, Varner JA. Regulation of angiogenesis *in vivo* by ligation of integrin $\alpha_5\beta_1$ with the central cell-binding domain of fibronectin. Am J Pathol 2000;156:1345–62.
10. Marchiò S, Lahdenranta J, Schlingemann RO, et al. Aminopeptidase A is a functional target in angiogenic blood vessels. Cancer Cell 2004;5:151–62.
11. Kolonin MG, Pasqualini R, Arap W. Teratogenicity induced by targeting a placental immunoglobulin transporter. Proc Natl Acad Sci U S A 2002;99:13055–60.
12. Yao VJ, Ozawa MG, Trepel M, Arap W, McDonald DM, Pasqualini R. Targeting pancreatic islets with phage display assisted by laser pressure catapult microdissection. Am J Pathol 2005;166:625–36.
13. Koivunen E, Wang B, Ruoslahti E. Phage libraries displaying cyclic peptides with different ring sizes: ligand specificities of the RGD-directed integrins. Bio/Technology 1995;13:265–70.
14. Ellerby HM, Arap W, Ellerby LM, et al. Anti-cancer activity of targeted pro-apoptotic peptides. Nat Med 1999;5:1032–8.
15. Arap W, Pasqualini R, Ruoslahti E. Cancer treatment by targeted drug delivery to tumor vasculature in a mouse model. Science 1998;279:377–80.
16. Zitzmann S, Ehemann V, Schwab M. Arginine-glycine-aspartic acid (RGD)-peptide binds to both tumor and tumor-endothelial cells *in vivo*. Cancer Res 2002;62:5139–43.
17. Folkman J. Endogenous angiogenesis inhibitors. APMIS 2004;112:496–507.
18. Hicklin DJ, Ellis LM. Role of the vascular endothelial growth factor pathway in tumor growth and angiogenesis. J Clin Oncol 2005;23:1–17.
19. Dash AB, Williams IR, Kutok JL, et al. A murine model of CML blast crisis induced by cooperation between BCR/ABL and NUP98/HOXA9. Proc Natl Acad Sci U S A 2002;99:7622–7.
20. Erber R, Thurnher A, Katsen AD, et al. Combined inhibition of VEGF and PDGF signaling enforces tumor vessel regression by interfering with pericyte-mediated endothelial cell survival mechanisms. FASEB J 2004; 18:338–40.
21. Bergers G, Song S, Meyer-Morse N, Bergsland E, Hanahan D. Benefits of targeting both pericytes and endothelial cells in the tumor vasculature with kinase inhibitors. J Clin Invest 2003;111:1287–95.
22. Holash J, Davis S, Papadopoulos N, et al. VEGF-Trap: a VEGF blocker with potent antitumor effects. Proc Natl Acad Sci U S A 2002;99:11393–8.
23. Wickman G, Hallin M, Dillon R, et al. Further characterization of the potent VEGF/PDGF receptor tyrosine kinase inhibitor, AG013736, in preclinical tumor models for its antiangiogenesis and antitumor activity. Proc Am Assoc Cancer Res 2003;44:A3780.
24. Inai T, Mancuso M, Hashizume H, et al. Inhibition of vascular endothelial growth factor (VEGF) signaling in cancer causes loss of endothelial fenestrations, regression of tumor vessels, and appearance of basement membrane ghosts. Am J Pathol 2004;165:35–52.
25. Pietras K, Hanahan D. A multitargeted, metronomic, and maximum-tolerated dose "chemo-switch" regimen is antiangiogenic, producing objective responses and survival benefit in a mouse model of cancer. J Clin Oncol 2005;23:939–52.
26. Willett CG, Boucher Y, di Tomaso E, et al. Direct evidence that the VEGF-specific antibody bevacizumab has antivascular effects in human rectal cancer. Nat Med 2004;10:145–7.
27. Winkler F, Kozin SV, Tong RT, et al. Kinetics of vascular normalization by VEGFR2 blockade governs brain tumor response to radiation: role of oxygenation, angiopoietin-1, and matrix metalloproteinases. Cancer Cell 2004;6:553–63.
28. Jain RK. Normalization of tumor vasculature: an emerging concept in antiangiogenic therapy. Science 2005;307:58–62.
29. Hanahan D. Heritable formation of pancreatic β-cell tumours in transgenic mice expressing recombinant insulin/simian virus 40 oncogenes. Nature 1985;315: 115–22.
30. Zacher AN III, Stock CA, Golden JW II, Smith GP. A new filamentous phage cloning vector: fd-tet. Gene 1980;9:127–40.
31. Smith GP, Scott JK. Libraries of peptides and proteins displayed on filamentous phage. Methods Enzymol 1993;217:228–57.
32. Pasqualini R, Arap W, Rajotte D, Ruoslahti E. *In vivo* selection of phage display libraries. In: Barbas CF III, Burton DR, Scott JK, Silverman GJ, editors. Phage display: a laboratory manual. Cold Spring Harbor (New York): Cold Spring Harbor Laboratory Press; 2001. p. 22.9.
33. Ruoslahti E. RGD and other recognition sequences for integrins. Annu Rev Cell Dev Biol 1996;12:697–715.
34. Parsons-Wingerter P, Kasman IM, Norberg S, et al. Uniform overexpression and rapid accessibility of $\alpha_5\beta_1$ integrin on blood vessels in tumors. Am J Pathol 2005;167:193–211.
35. Magnussen A, Kasman IM, Norberg S, Baluk P, Murray R, McDonald DM. Rapid access of antibodies to $\alpha_5\beta_1$ integrin overexpressed on the luminal surface of tumor blood vessels. Cancer Res 2005;65: 2712–21.
36. Byzova TV, Goldman CK, Pampori N, et al. A mechanism for modulation of cellular responses to VEGF: activation of the integrins. Mol Cell 2000;6: 851–60.

37. Soldi R, Mitola S, Strasly M, Defilippi P, Tarone G, Bussolino F. Role of $\alpha_v\beta_3$ integrin in the activation of vascular endothelial growth factor receptor-2. EMBO J 1999;18:882–92.
38. Davis GE, Camarillo CW. An $\alpha_2\beta_1$ integrin-dependent pinocytic mechanism involving intracellular vacuole formation and coalescence regulates capillary lumen and tube formation in three-dimensional collagen matrix. Exp Cell Res 1996;224:39–51.
39. Senger DR, Claffey KP, Benes JE, Perruzzi CA, Sergiou AP, Detmar M. Angiogenesis promoted by vascular endothelial growth factor: regulation through $\alpha_1\beta_1$ and $\alpha_2\beta_1$ integrins. Proc Natl Acad Sci U S A 1997;94:13612–7.
40. Giancotti FG, Ruoslahti E. Integrin signaling. Science 1999;285:1028–32.
41. Christofori G, Naik P, Hanahan D. Vascular endothelial growth factor and its receptors, flt-1 and flk-1, are expressed in normal pancreatic islets and throughout islet cell tumorigenesis. Mol Endocrinol 1995;9:1760–70.
42. Hwang R, Varner J. The role of integrins in tumor angiogenesis. Hematol Oncol Clin North Am 2004;18: 991–1006.
43. Morikawa S, Baluk P, Kaidoh T, Haskell A, Jain RK, McDonald DM. Abnormalities in pericytes on blood vessels and endothelial sprouts in tumors. Am J Pathol 2002;160:985–1000.
44. Ozawa MG, Yao VJ, Chanthery YH, et al. Angiogenesis with pericyte abnormalities in a transgenic model of prostate carcinoma. Cancer 2005;104:2104–15.
45. Smith GP. Filamentous fusion phage: novel expression vectors that display cloned antigens on the virion surface. Science 1985;228:1315–7.
46. Kolonin MG, Saha PK, Chan L, Pasqualini R, Arap W. Reversal of obesity by targeted ablation of adipose tissue. Nat Med 2004;10:625–32.
47. Zurita AJ, Troncoso P, Cardó-Vila M, Logothetis CJ, Pasqualini R, Arap W. Combinatorial screenings in patients: the interleukin-11 receptor α as a candidate target in the progression of human prostate cancer. Cancer Res 2004;64:435–9.
48. Joyce JA, Laakkonen P, Bernasconi M, Bergers G, Ruoslahti E, Hanahan D. Stage-specific vascular markers revealed by phage display in a mouse model of pancreatic islet tumorigenesis. Cancer Cell 2003;4: 393–403.
49. Essler M, Ruoslahti E. Molecular specialization of breast vasculature: a breast-homing phage-displayed peptide binds to aminopeptidase P in breast vasculature. Proc Natl Acad Sci U S A 2002;99:2252–7.